Constraining crustal and sedimentary structure of Southeast Australia with Rayleigh wave ellipticity

Haoming Wu

Department of Earth and Planetary Sciences,
Macquarie University

A thesis submitted in partial fulfilment of the requirements for the degree of
Master of Research

MACQUARIE
University

Abstract

Ambient noise tomography has been widely applied in seismic studies to invert for crustal and upper mantle structure, but has limited resolution for the near surface layer. A recent method involves measuring the ellipticity or ZH ratio of Rayleigh waves to further constrain shallow sedimentary structure. We apply this method to South-East Australia, using multicomponent ambient noise data obtained from the WOMBAT array. We present a shear wave velocity model, derived from the joint inversion of Rayleigh wave ZH ratio and phase velocities measured at short periods (2-10s). At shallow depth, our shear wave velocity model showed strong spatial correlation with the known surface geology. High velocities were associated with the Gawler craton and the eastern subprovince of the Lachlan Orogen. This contrasted with anomalously low velocities featured prominently in the locations of the Central Murray basin, Sydney Basin and the Northern Curnamona province at 1km depth. A low velocity, shallow layer of 0.5-2km thickness was detectable across study region, which was found to be thicker beneath sedimentary basins. We evaluate the strengths and limitations of the ZH ratio method for the South-East Australia dataset.

Acknowledgements

Statement of originality

The work presented in this thesis is my original work and has not been submitted for any award at another university or institution. I certify that the material presented here has not been presented or published elsewhere, except where acknowledged in the text.

Haoming Wu
Author, MRES Candidate

Contents

Table of Figures

1.1 Introduction

For over a decade, ambient noise tomography has seen widespread application in studying the structure of the Earth's crust and upper mantle. Ambient noise methods have advantages over traditional surface wave tomography mainly due to not relying on an active source (e.g. Earthquakes) to acquire data (Shapiro et al., 2005). Instead, ambient seismic noise techniques harness random seismic noise which is ubiquitously observed at seismic receivers. This makes it an ideal method for relatively aseismic regions such as Australia. By cross-correlating and stacking the recorded noise between two stations, we can extract the Empirical Greens Function. This Green's function can be measured to obtain the group and phase speeds of the Rayleigh wave travel path, between the station pair (Bensen et al., 2007).

The increasing prevalence of dense, continental-scale seismic arrays have allowed very high-resolution images to be obtained from ambient noise. The most extensive ambient noise studies are located in the Western United States using the Earthscope array (Ritzwoller et al., 2011) where some of the first ambient noise studies were performed (Shapiro and Campillo, 2004). Despite its successes, ambient noise techniques have limitations in constraining near-surface structure (Li et al., 2016), particularly for the top 5 kilometres (Lin et al., 2014).

The newfound availability of multicomponent seismic data in concentrated arrays has enabled the measurement of the radial components of Rayleigh waves. In recent years, this has been used to calculate the ellipticity or ZH ratio of Rayleigh waves (Tanimoto and Rivera, 2008). This parameter has been found to be more sensitive to shallow depth compared to phase velocity, and provides independent constraints on structure (Chong et al., 2014). Therefore, the joint inversion of these measurements can be used to study shallower structures in greater detail. This unique methodology has not yet been applied in Australia, where we have multicomponent data from a dense seismic array in south-east Australia (Tkalcic et al., 2012).

The importance of studying shallow seismic structure is related to acquiring more subsurface spatial data, especially about economically significant areas. In South-East Australia we have the Broken Hill and Olympic Dam deposits, which contain mineralization of prime economic importance (Conor and Preiss, 2008). Sedimentary basins such as Sydney Basin are rich in hydrocarbons and have also been

studied for geothermal potential (Danis et al., 2011). In addition, determining basin structure is critical for evaluating seismic hazards because basins amplify strong seismic motion (Ma et al., 2016). Lastly, the results of our model should provide some more information about near-surface geology that should aid future interpretations when extrapolating to depth. Measurement ZH ratio does not require any unique instrumentation to be deployed since the multicomponent data is already available for most of NSW and South Australia.

1.2 Background

1.2.1 ZH Ratio

Firstly, we must clarify our definition of ZH ratio and what physical property it is inherently measuring. The motion of Rayleigh wave travel can be simplified as having a circular or elliptical path, hence it is often referred to as "ground roll". Therefore, we can divide this motion into horizontal and vertical components of displacement (Malischewsky and Scherbaum, 2004). The Rayleigh wave ZH ratio simply refers to the ratio of vertical to horizontal amplitudes of displacement. This is measured as a local site property which is controlled by the 1-D structure beneath the receiver (Ma et al., 2016). Technically, it is the ratio of two vertical and horizontal eigenfunctions of Rayleigh waves at the surface, with the eigenfunctions controlled by local structure (Tanimoto and Rivera, 2008). Therefore, this measurement remains fixed for a given station. The ZH ratio is expected to show some azimuthal dependence given an anisotropic medium, but should remain constant for particular azimuths. It has been found that this ratio is particularly sensitive to shallow sediments, which will exhibit lower ZH ratios compared to basement (Lin et al., 2014). Due to these properties, it has been used to help constrain near-surface structure when jointly inverted with Rayleigh wave dispersion data (Li et al., 2016).

Measurement of ZH ratio requires seismometers capable of measuring 3 directional components of a wave arrival. This includes a vertical (Z-direction) and radial/horizontal components (X and Y direction). Tanimoto and Rivera (2008) demonstrates two methods to measure ZH ratio. To summarize, the first involves measuring the amplitude of the envelope functions in vertical and horizontal components, and taking the ratio between them. The second uses a waveform correlation technique between vertical and horizontal components. We will elaborate on the specific procedure we apply in the methods section.

The method we adopt here is not to be confused with traditional H/V analysis of raw noise spectra. Our interpretation of ZH ratio does not heavily rely on assumed noise character and the relationship to 1-D structure is well defined (Lin et al., 2014). Following Tanimoto and Rivera (2008), we represent our ratio as Z/H (Vertical over Horizontal), with the horizontal component as the denominator instead of the traditional H/V. The reason for this is that for certain structures, very small vertical amplitudes of

Rayleigh waves can make the H/V ratio numerically unstable. Defining it inversely removes this problem, ensuring that ZH ratio is always defined when inverting for Earth structure.

1.2.1.1   ZH Ratio Sensitivity

The effective depth sensitivity of ZH ratio has been a major focus of study in recent years with ambient noise. One of the earliest studies on ZH ratio was by Boore and Toksoz (1969), who found that near-surface sedimentary layers strongly influenced ZH ratio, more so than they did for phase velocities. They focused on short frequency bands (0.02-0.1Hz), using the LASA array in Montana, USA which provided the required station density and three component measurements. Their results demonstrated that ZH ratio and phase velocity measurements were independently influenced by structure. They made an unintended observation that ZH ratio was only highly sensitive to the near surface structure, highlighting this as a flaw. While both exhibited similar sensitivity for structural perturbations, the low-velocity, near surface sedimentary layers were found to be a much stronger influence on the ZH ratio.

From their result, we now know that ZH ratio has stronger sensitivity to near-surface structure. The sensitivities of these parameters were explored further by Chong et al. (2014), who conducted a forward modelling experiment to determine ZH ratio and phase velocity through a layered structure. While both were sensitive to changes in velocity in the crust, there was a strong difference in their pattern of sensitivity. Phase velocity showed a more averaged velocity for the sampled depth range while ZH ratio was more sensitive to shallower depth for the same frequencies. **Figure 1** shows the sensitivity kernels calculated by (Li et al., 2016) for ZH ratio and phase velocity, demonstrating the differences in depth sensitivity. Since each parameter holds independent constraints on structure, the joint inversion of these two datasets would provide improved constraints on the crustal structure and reduce non-uniqueness (Li et al., 2016).
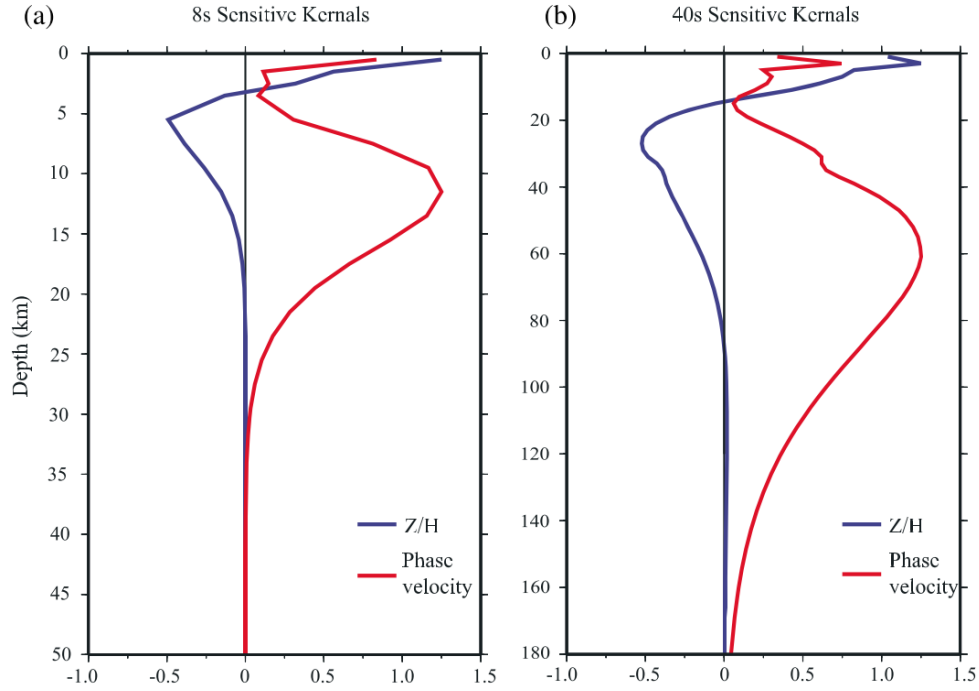
Figure 1: Comparison of sensitivity kernels for ZH ratio and Phase velocity at a) 8s, b) 40s. Obtained from (Li et al., 2016)

1.2.1.2 Recent Applications of ZH Ratio

Earlier studies demonstrated that ZH ratio provided independent constraints on shallower structure but were limited in their application. Regional-scale studies in recent years have jointly inverted ZH ratio and phase velocities to reduce non-uniqueness at shallow depth.

Lin et al. (2014) created a 3-D model of the Western United States using the joint inversion of ZH ratio and phase velocity from ambient noise. Through careful pre-processing, they were able to extract robust short-period ZH ratios from multicomponent ambient noise cross-correlations. These measurements were mostly concentrated in the 8-24s band which contained the strongest microseism energy. Their final 3-D shear velocity (Vs) model showed good agreement with known geology through most of the crust and upper mantle, and could resolve basalt flows overlying a sedimentary basin. It was the inclusion of short period H/V ratios that provided the necessary constraints to resolve structures as shallow as the top ~1km of the crust. Though the near-surface is highly heterogenous, this information allows for extrapolation of structure to the deeper parts of the crust. They not only demonstrated that Vs was obtainable from the joint inversion, but also density and Vp/Vs ratio.

Li et al. (2016) used the joint inversion of Rayleigh wave ZH ratio and phase velocity to acquire a velocity model of Northeast China for the periods 8-40s. They used both an earthquake and ambient noise dataset to conduct their measurements. The ZH ratios showed good spatial correlation with the known surface geology where it was observed to be lower in sedimentary basins compared to surrounding areas. The low-velocity anomalies of the northern and southern Songliao basin extended to varying depth of up to 3km difference. The difference was suggested to be caused by mantle upwelling, due to subduction of the Pacific plate. As well as being consistent with previous models, the shallower structures showed a stronger spatial correlation with the main tectonic terranes. Overall, this study demonstrated the high effectiveness of using ZH ratio measurements to distinguish sedimentary basins from the surrounding terranes.

1.2.2 Geological Setting

The area of study comprises most of New South Wales (NSW) and extends west into part of South Australia **(Figure 2)**. The NSW region primarily features the Tasmanide orogenic belts as the main tectonic terranes as well as hosting the Sydney-Gunnedah and Murray-Darling sedimentary basin systems. The key features of interest in South Australia are the Gawler craton and Curnamona province. In this section, we will provide a brief description of these units and review some of the perspectives on their tectonic evolution.
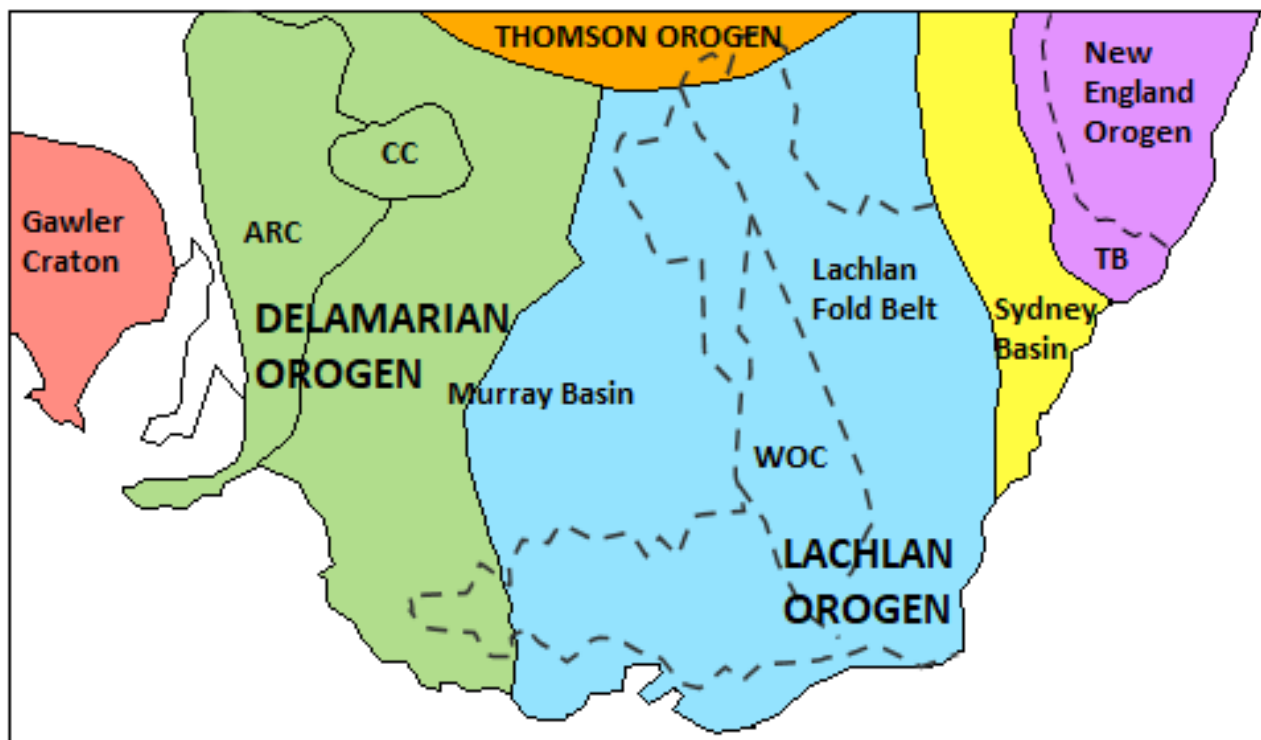
Figure 2: *Simplified Geological map of South-East Australia showing the main tectonic units*
Solid lines represent boundaries between the major orogens. Dashed lines outline surface geological features. ARC=Adelaide Fold Complex, CC=Curnamona Craton, WOC=Wagga-Omeo Complex, TB=Tasman Belt. Adapted from Gray and Foster (2004) and Glen (2013).

1.2.2.1 The Tasmanides

The Tasmanides in our study region include the Delamerian, Lachlan and New England orogens (formed in respective order), which form a margin of large-scale continental accretion along Eastern Australia and date from the Early Cambrian to Mesozoic (Glen et al., 2009). The breakup of Rodinia triggered the formation of these orogenic belts along the eastern margin of Gondwana, all while the paleo-Pacific plate was moving east (Glen, 2005). Accretionary orogens track the growth of a continental landmass by the gradual accumulation of island arcs, ocean crust, continental fragments and sedimentary terranes (Glen, 2013). This involves a style of oceanic-continental convergent margin tectonics where buoyant exotic crustal material is transferred from the downgoing plate into the overriding plate. Additionally, the overriding plate is subjected to crustal extension and back-arc basin development driven by slab rollback. (Moresi et al., 2014).

The Delamerian Orogen is located in the western portion of NSW and contains rocks that have undergone multistage mid-late Cambrian to Ordovician deformation (Glen, 2005). It is suggested that the Delamarian orogen was formed from west-dipping subduction along the East Gondwana margin (Foden et al., 2006). The western part of the orogen includes the Adelaide fold belt, which underwent contractional orogenesis at ~514-490Ma, and ended through rapid uplift, cooling and extension associated with post-tectonic magmatism. The eastern part of the Delamerian consists of multiply-deformed and metamorphosed sediments that developed from inversion of the Cambrian deepwater Kanmantoo Trough (Glen, 2005). Paleoproterozoic and Mesoproterozoic crust forms the basement of this orogen and is suggested to be connected to the Curnamona craton.

The Lachlan Orogen covers most of the south-eastern portion of Australia, and was once part of a Paleozoic convergent plate margin. The Lachlan fold belt is described to be a retreating subduction zone orogen and is largely composed of deformed quartz-rich turbidites, cherts and mafic volcanic rocks of Cambrian to Devonian age (Foster and Gray, 2000). The prevalence of turbidites is a deep-marine feature which is thought to be part of an ancient submarine sediment dispersal system. Much of the difficulty of understanding the Lachlan is due to the presence of younger Mesozoic-Cainozoic sedimentary and volcanic cover sequences which mask a large portion of the Paleozoic basement (Foster and Gray, 2000). This has also made the boundaries between orogens difficult to infer. The location and definition of the boundaries between the orogens is still a contentious issue, particularly

between the Delemarian and Lachlan (Glen, 2013). Early studies defined this boundary as the Avoca fault in Victoria, but currently the Moyston fault further west is preferred and supported by seismic studies (Rawlinson et al., 2011).

The New England Orogen is located in the north-east of NSW, forming part of the basement for the Sydney Basin. This represents the youngest segment of the Tasmanides. Here there is inferred to be thrust contact with the Eastern subprovince of the Lachlan Orogen (Glen, 2005). Only the southern portion of the New England Orogen is featured in our dataset but it is nonetheless important to investigate its structure in relation to the Lachlan orogen and Sydney Basin.

1.2.2.2 Gawler and Curnamona

The Gawler craton is made up of a Late Archaen-Early Paleoproterozoic nucleus which is surrounded and intruded by Paleoproterozoic and Mesoproterozoic lithologies (Payne et al., 2008). Much of the Late Archaen stratigraphy includes metasedimentary, volcanic and granite-greenstones that have undergone extensive deformation. The evolution of the Gawler craton is marked by two major tectonic cycles between ~2560 Ma ~1450 Ma which include volcano-sedimentary basin formation, collisional and extensional deformation and magmatic emplacement followed by regional cooling (Pilia et al., 2013). Most of the craton is covered by Neoproterozoic and Phanerozoic sediments (Payne et al., 2008). As with other cratonic regions in Australia, the Gawler craton is associated with faster seismic velocities (Saygin and Kennett, 2012). It is here that we should expect to see a transition from Phanerozoic east-Australian units into Proterozoic sediments and Archaen basement along the Tasman line. Defining location of this transitory line has been the focus of previous seismic studies in the region (Kennett et al., 2004, Rawlinson et al., 2014) .

The circular-shaped Curnamona province lies within the Delamarian Orogen and hosts the Paleoproterozoic Willyama Supergroup. This highly-deformed and metamorphosed group was deposited by epi-continental rifting that was accompanied by extensive magmatism (Conor and Preiss, 2008). It is suggested that the Curnamona province and Gawler craton were once part of the same contiguous crust prior to the Neoproterozoic but are now separated by the Adelaide Rift Complex (Pilia et al., 2015). Most of the Curnamona is buried under Mesozoic-Quartenary cover (Rawlinson et al., 2014).
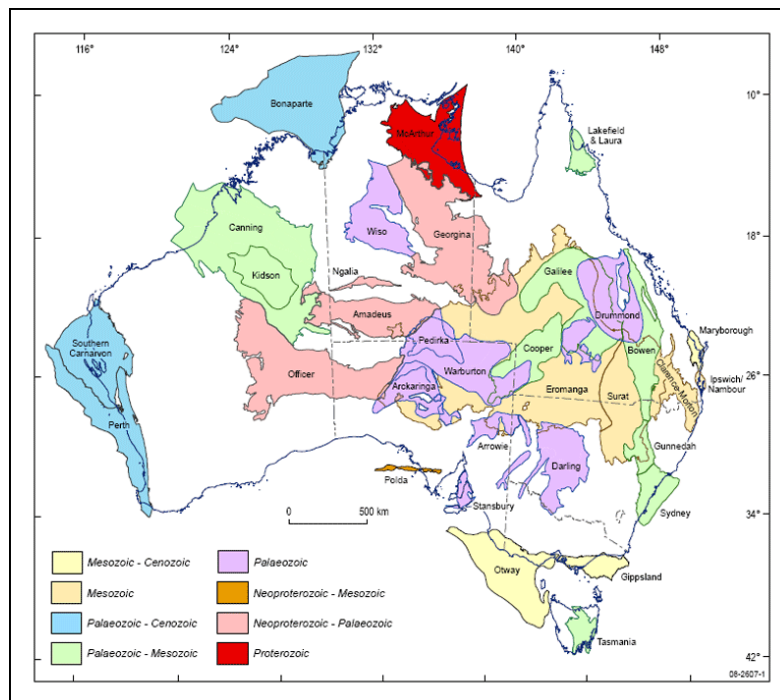
1.2.2.3 Sedimentary Basins

The two major sedimentary basins in our data region are the Sydney and Murray basins in NSW. The northernmost point of our dataset, in the Curnamona province, lies partly in the Arrowie and Eromanga basins. We expect to find some delineation of these sedimentary features from our tomographic model especially with additional constraints from ZH ratio. **Figures 3a** and **3b** show the extent of the major sedimentary basins and estimates of sedimentary thickness respectively.

The Sydney Basin System is one of the main sedimentary features in the study region, located between the Lachlan and New England orogens. As can be in in **Figure 2**, this system extends into Queensland via the Gunnedah and Bowen basins. The Sydney basin originated by early Permian rifting and was converted into a basin foreland in the mid-Triassic, with the eastern parts forming the foreland fold-thrust belt of the New England Orogen (Glen, 2005). The sedimentary profile includes both marine and terrestrial formations that comprise of sandstones, shales, claystones and coal with the added presence of extrusive volcanics and late intrusive plutons. Sedimentary thicknesses of 4800m to 9000m are estimated for the onshore Sydney Basin (Danis et al., 2011).

The Murray Basin forms most of the sedimentary cover overlying both the Delamarian orogen and the western part of the Lachlan orogen. The Murray is an intracratonic basin containing a thin layer of Cenozoic sediments (200-400m) with a maximum thickness of 600m in the deepest parts of the basin (Brown and Stephenson, 1991). This blanket of sediments extends over a vast area where it unconformably overlies the Willyama block to the north-west and the sedimentary rocks of the Darling Basin in the north. Here, the Darling refers to a smaller Paleozoic basin which is overlain by the much larger Murray basin. The subsidence of the Murray basin began in the early Tertiary which diverted its north-flowing drainage pattern away from the Eromanga basin (Ollier, 1995). Folded and partly metamorphosed Proterozoic and Lower Paleozoic rocks make up the basement of the Murray basin (Brown and Stephenson, 1991).

a)

b)
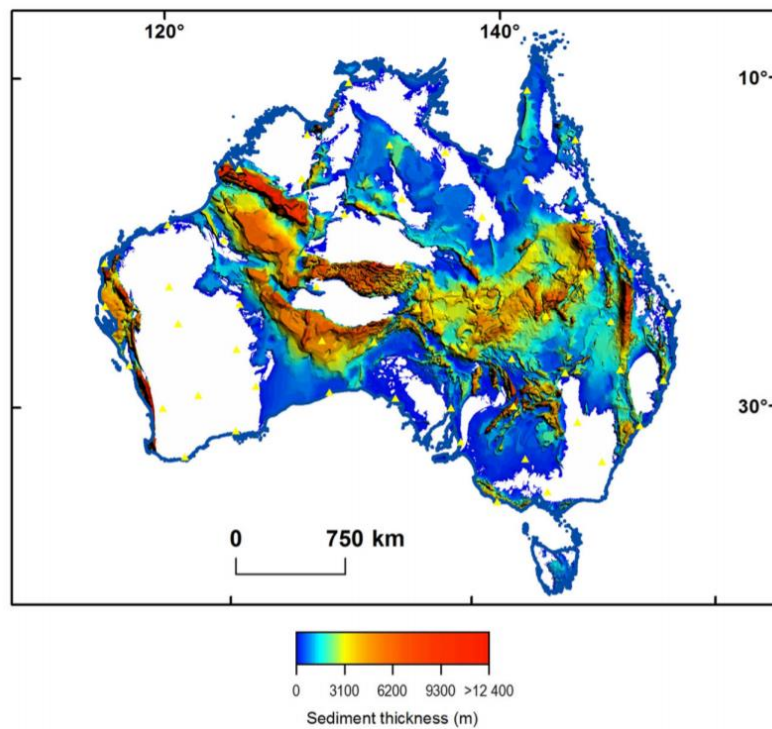
Figure 3: Maps showing sedimentary basin extent in Australia
a) Locations and ages of major onshore basins, b) Sedimentary thickness estimates. Courtesy of ©
Commonwealth of Australia (Geoscience_Australia, 2012) and (Wang et al., 2014).

1.2.3 History of WOMBAT Studies

Previous seismic tomography studies of South-East Australia have made extensive use of the WOMBAT array. The WOMBAT Array is a temporary transportable seismic array that has been sequentially expanded over the past two decades, most prominently by researchers at the Research School of Earth Science, Australian National University. This was undertaken with the objective of achieving coverage of most of the Australian continent, allowing detailed seismic studies to be conducted. Most of the array is centered on south-east Australia, maintaining an average station spacing of 50km (Tkalcic et al., 2012).

While many earlier surface wave tomography studies in Australia imaged on the continental-scale (Simons et al., 1999) (Saygin and Kennett, 2010), more recent focus has been on higher density, localized arrays targeting specific geological regions. Such studies include imaging the crust and mantle beneath Southeast Australia (Rawlinson et al., 2014, Arroucau et al., 2010, Tkalcic et al., 2012, Young et al., 2013) and Tasmania (Young et al., 2011). These studies comprise a variety of ambient noise and teleseismic receiver function methods. This has also led to the development of methods for joint inversion of receiver functions with surface wave dispersion (Bodin et al., 2012). Conveniently, receiver function techniques require three-component seismograms, which is also a requirement for the ZH ratio method we have adopted.

Group velocities maps derived from these studies have shown low velocity anomalies corresponding to sedimentary basins and recent hot-spot volcanism. High velocities are generally associated with metamorphic and igneous outcrop (Arroucau et al., 2010). There has also been observed high wave speeds in the Delamerian Orogen as well as the Wagga-Omeo complex in NSW (Rawlinson and Kennett, 2008). More recently, a comprehensive P-wave model of the crust and upper mantle has shown negative velocity anomalies in the lower crust beneath the Gawler and Curnamona province (Rawlinson et al., 2016). The most directly comparable study to ours in terms of the data and methodology is Young et al. (2013), who inverted phase velocities for crustal structure in South-East Australia. A key feature of their model was the distinct illumination of the Torrens Hinge Zone and Boothragandra Fault at mid-crustal depths. Similarly, Pilia et al. (2015) detects the Bootheragndra Fault across many depths in their model, where it acts as a margin that separates complex units beneath the Lachlan.

1.3   Aims

In this section, we have considered the relatively novel status of seismic tomography research involving ZH ratios and have outlined the present understanding of southeast Australia tectonics. It has become clear that using ZH ratios derived from the multicomponent seismic array in this region, we can obtain a greater spatial understanding of the shallow structure. Based on this, we have three aims which we hope to achieve with this project:

- o   Develop a shear wave velocity model of the South-Australian crust from 1-D joint inversion of ZH ratio and phase velocity measurements
- o   Apply our tomographic model to make some interpretations about the crustal and sedimentary structure of south-east Australia
- o   Evaluate the effectiveness of ZH ratios to constrain shallow crustal structure and sedimentary features

2. Methodology

2.1 Data Source

The WOMBAT array contains a multitude of smaller, concentrated subarrays that have been sequentially deployed over several decades. The array comprises a total of over 400 seismic stations across South-East Australia with an approximately 50km spacing (Tkalcic et al., 2012). We use the broadband stations capable of recording multicomponent data, shown in **Figure 4**, which belong primarily to the most recent set of deployments: the SEAL2, SEAL3, GW, CU, EAL2, EAL2, and EAL3 subarrays. This makes a combined total of 294 stations distributed across New South Wales and reaching as far west as the Gawler craton in South Australia.
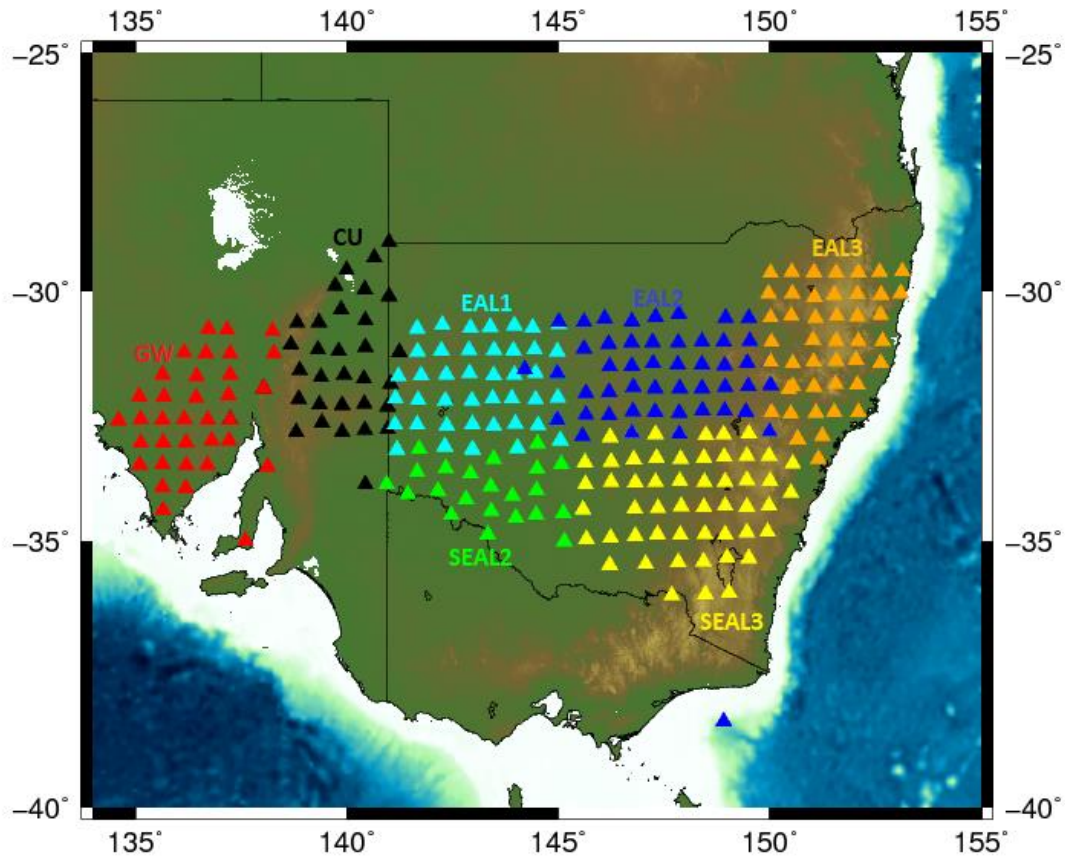
Figure 4: *Map of WOMBAT array stations used for this study*
The triangles represent the multicomponent seismic stations composed of the subarrays: GW, CU, EAL1, EAL2, EAL3, SEAL2, SEAL3. Aside from some overlap between SEAL3 and GW, each subarray was deployed in a different time period.

2.2 Data Processing

To obtain the desired Green's functions, we follow the standard ambient noise data processing method outlined by Bensen et al. (2007), with some modifications for processing 3 directional components (Z, N, E) and measurement of ZH ratio. This consists of 5 main steps: Single station data preparation, cross-correlation and stacking, measurement of dispersion curves measurement of ZH ratio, and quality control.

2.2.1 Single station preparation

Single-station data preparation involves editing the raw data to remove irregularities and prepare it for the cross-correlation step. This is important to ensure that imbalances in the data do not negatively affect the final outcome. A standard procedure is applied to all three components for each station. To begin, the raw seismic seed data is required to be converted into a readable sac format. During this step, the instrument response, the mean and the linear trend are removed (Bensen et al., 2007). The signal is then decimated to a sample rate of 1Hz as per (Li et al., 2016), to minimise the required processing time without under-sampling the data. The data is also cut between 300 and 86100 points to align the start and end times.

Temporal normalization and spectral whitening are the more crucial parts of the pre-processing step and are simultaneously applied to all three components. Temporal normalization aims to suppress irregular signals in the data, especially those caused by earthquakes, but also instrument irregularities and moving noise sources nearby to stations (Bensen et al., 2007). The effect of earthquakes is usually greatest after the 15s periods, past the microseism band (~5-17s). Firstly, A bandpass filter is fixed from 5s to 50s. We apply the specific normalization method employed by Lin et al. (2014), which involves computing a running average in a time window of 64s. For each station and time, the unfiltered three component noise recordings are divided by the maximum of the temporal normalization functions. Finally, we apply spectral whitening to smooth out peaks in the primary and secondary microseisms (Bensen et al., 2007). The spectrum of each component is divided by the average of the three-component smoothed spectrum (Lin et al., 2014). Doing so broadens the band of ambient noise, reducing imbalances caused by spectral peaks.

2.2.2 Cross-correlation and stacking

The Cross-correlation step is performed next and is crucial to retrieving the desired Green's function after sufficient averaging or stacking. Cross-correlation essentially accumulates small contributions over time from noise sources passing through both stations (Shapiro et al., 2005). In our case, there is a total of 9 cross-correlation functions to compute between each station pair and their components: ZZ, ZE, ZN, EE, EN, EZ, NN, NE, and NZ (Li et al., 2016). The first letter here refers to the virtual source, followed by the receiver. The stacking is done as a single step to combine all the cross-correlations for each individual day, into one sac file. Each subarray is stacked for at least one year's worth of data, between the years 2007 to 2011.

Proceeding the cross-correlation step is rotation. Rotating the north and east components into the radial makes further computation more efficient as well as saving space (Lin et al., 2008). This involves a matrix calculation based on the virtual source and receiver geometry (Li et al., 2016, Lin et al., 2008):

$$
\begin{pmatrix} ZZ \\ ZR \\ RZ \\ RR \end{pmatrix} = \begin{pmatrix} 1 & 0 & 0 & 0 & 0 & 0 & 0 & 0 & 0 \\ 0 & cos\psi & sin\psi & 0 & 0 & 0 & 0 & 0 & 0 \\ 0 & 0 & 0 & -cos\theta & 0 & 0 & -sin\theta & 0 & 0 \\ 0 & 0 & 0 & 0 & -cos\theta cos\psi & -cos\theta sin\psi & 0 & -sin\theta cos\psi & -sin\theta sin\psi \end{pmatrix} \begin{pmatrix} ZZ \\ ZN \\ ZE \\ NZ \\ NN \\ NE \\ EZ \\ EN \\ EE \end{pmatrix} \quad (1)
$$

Here, the coefficients refer to the angles of the interstation azimuth (θ), at the virtual source, and backazimuth (ψ), at the receiver. We see that the rotation of the 9 cross-correlation components produces a total of 4 radial (R) and transverse (Z) components.

2.2.3 Measurement of dispersion curves

After a Green function is obtained from cross-correlations, the group and phase speeds as a function of period can be measured using automated frequency-time analysis (FTAN), resulting in a dispersion curve (Bensen et al., 2007). In FTAN, a 2-D diagram of signal power is created, as a function of time and the central frequency of the applied filters (Yang et al., 2007). The local power maximum is tracked along the frequency axis and the raw group velocity curve is calculated from the group arrival times at maximum amplitude. This initial procedure is followed by steps to clean the waveform of potential

contamination (Bensen et al., 2007). This involves applying several filters including phase-matched and anti-dispersion filters. The filtered signal is redispersed by applying the inverse of the phase-matched filter to it (Levshin and Ritzwoller, 2001). The final group and phase velocity curves can then be obtained from the cleaned image. We use a phase velocity reference model based on the model of (Young et al., 2013), to solve the 2π phase ambiguity in the phase measurement.

2.2.4 Measurement of ZH ratio

After calculating noise-correlation functions for each virtual source-receiver pair, they are stacked from a vertical and radial source to enhance Signal-to-noise Ratio (SNR) when measuring ZH ratio. The measured ZH ratio for the positive part is expected to correspond to the velocity structure beneath the receiver (Li et al., 2016). By extension, the negative part corresponds to velocity structure beneath the virtual source. From (1), the ZZ and ZR components signify the vertical force while the RZ and RR components represent the radially directed force. To measure the ZH ratio, we are comparing the maximum amplitudes (A) of these components:

$$E(T) = \frac{A_{ZZ}}{A_{ZR}} = \frac{A_{RZ}}{A_{RR}} = \frac{A_{(H[ZZ]+RZ)}}{A_{(H([ZZ]+RR)}} \qquad (2)$$

H[ZZ] represents the Hilbert transform of the ZZ noise correlation function, which is applied to keep these two components in phase. This leaves us with the problem of RZ and ZR being out of phase.

Our specific method for calculating ZH, adapted from Tanimoto and Rivera (2008) and Li et al. (2016), takes advantage of the known fact that there is a 90° phase shift between the Z and R components. i.e. ZZ and RR are in phase while ZR is 90° ahead and RZ is 90° behind. For a selected Rayleigh wave time window, we apply a narrow bandpass filter centred at 0.025Hz. We then compute the zero-lag cross-correlation coefficient of the phase-advanced vertical component and the phase-delayed radial component. The data is discarded if this coefficient is <0.8. If kept, we compute the envelope function of the two components and the maxima of these are used to calculate the ZH ratio.

2.2.5 Quality Control

Finally, the quality control step involves identifying and rejecting poor quality measurements while computing statistics for the accepted measurements (Bensen et al., 2007). In order to perform our inversions with sufficient accuracy, the data we have processed is subjected to stringent quality control criteria. Some standard procedure for computing acceptable data is as follows (Lin et al., 2014):

- o To satisfy the far-field approximation, remove all virtual source stations within three wavelengths of the target stations.
- o Remove all virtual source stations with SNR < 8 on any of the four components.
- o Remove virtual source stations with inconsistent (>1 period) Rayleigh-wave phase traveltime when comparing ZR, RZ and RR to traditional phase traveltime derived from the ZZ cross-correlation.

For ZH ratios, measurements are also subjected to the same first two criteria but also include a requirement of at least 20 measurements to get a statistically robust average (Li et al., 2016). The distribution of Z/H measurements should roughly follow a Gaussian distribution with standard error <15% of the average. Any stations with less than 5 robust average Z/H estimates are discarded. This step is done simultaneously with the automated measurement of ZH ratio.

2.3 Phase Velocity Tomography

After processing our data and subjecting it to the quality control criteria, we can process the measured dispersion curves to create a 2D velocity model. Suitable raypaths are calculated from the previous quality control step, which primarily evaluated their SNR. The tomography program (Barmin et al., 2001) first assesses each raypath between stations for every period, based on their fit to a smoothed model. Any measurement that deviates too greatly from this initial simplified model is rejected as a bad measurement. The remaining measurements are used to do the final tomography. **Figure 5** summarises the number of accepted measurements compared to those rejected across the periods. The greatest path density is around the 5s period. We find that periods higher than 10s lack the required coverage to run the tomography as they contained <100 paths.
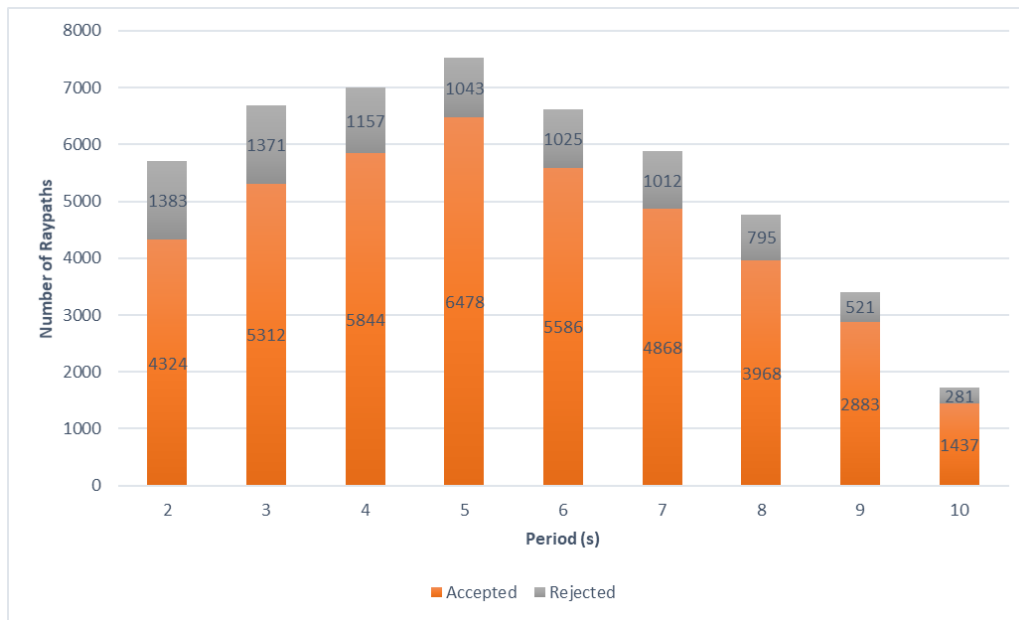
Figure 5: Number of accepted and rejected raypaths by period (2-10s)

The program inverts dispersion measurements for a regional 2-D map of surface wave velocity and requires appropriate parameterization (Barmin et al., 2001). There are two main variables which are important in deciding the output of the model, α and σ. These represent the smoothing and dampening coefficients respectively. From evaluating many different combinations of these values, α = 450, σ = 70 are chosen to be the most appropriate, as they provide a well smoothed model while retaining adequate detail within the inferred units.

The final model which is generated contains averaged values of phase velocity at each period. This could be mapped and interpolated onto a 2-D grid. The values for each 0.5° spaced grid point is extracted to create the input data file for the joint inversion in the next section.

2.4 Joint Inversion

We use the LITMOD program to invert for our 1-D shear velocity models. We adopt the joint inversion method for ZH ratio used by Li et al. (2016) which is a DRAM (Delayed Rejection Adaptive Metropolis) algorithm method. This is a type of Bayesian Markov chain Monte Carlo (MCMC) inversion. The Bayesian method creates a suite of models representing a posterior probability distribution that measures the degree of belief in a real Earth structure or composition (Bodin et al., 2012). It does this by comparing all random models with "a priori" information and observed data. The DRAM variant of this method differs in that it updates the probability of acceptance at a regular interval, which is determined by previous samples in the chain. This could lead to sampling regions with high posterior probability (Li et al., 2016).

The inversion requires two main inputs: a data file containing phase velocities and ZH ratio with period and a parameter file containing model constraints such as those shown in **Table 1**. The parameters control the effects of each layer in the Earth from the sediment, crust and mantle as well as including a range for the MOHO depth. The sediment thickness reference model is taken from Laske (1997). We estimate the average MOHO depth range for this part of the crust from the AusMOHO dataset (Kennett et al., 2011). In addition to these parameters are a set of cubic B splines describing velocities for both the crust and upper mantle (top 80km) and lower mantle (80-200km) which are taken from Li et al. (2016) and the Preliminary Reference Earth Model (PREM) (Dziewonski and Anderson, 1981) respectively.

Parameter	Range
Sediment Thickness	1.5-3.5$m0$
Vs range for top sediment layer	0-2.0km/s
Vs range for bottom sediment layer	0.5-3.0km/s
Vs range for crust	2.5-4km/s
MOHO depth range	30-40km/s

Table 1: Parameterization of the model space.
Here, m0 refers to the reference model from which our parameter is allowed to vary by the stated value.

We discretize our model space into a 0.5° by 0.5° grid between 132.0 to 154.0 longitude and -28.0 to -38.0 latitude. This includes a total of 945 points for which we run the 1-D inversion, using data extracted from interpolated maps of phase velocity and ZH ratio. Each point on these smoothed maps typically reflects an averaged value of ZH ratio observed in the nearest few stations. The method calculates 80,000 models for every point in our grid and select 3000 models with the smallest misfit. The misfit of the joint inversion (M_J) is determined by comparing the predicted (G) and observed phase velocities (D) at period (i), following the equation described by Li et al. (2016):

$$M_J = c_1 \cdot \sum_{i=1}^{N} \frac{[G_i(m) - D_i^{obs}]^2}{\sigma_i^2} + c_2 \cdot \sum_{j=1}^{M} \frac{[R_j(m) - B_j^{obs}]^2}{\gamma_j^2} \qquad (3)$$

Similarly, $R_j(m)$ describes the calculated ZH ratio and from model (m) at period (j) on a discrete grid (M). The uncertainties of the phase velocities and ZH ratios are represented by σ_i and γ_j respectively. Finally, the weighting factors of the two datasets (c_1, c_2) are set to be equal. The 3000 selected models are averaged to obtain the final 1-D shear wave velocity profile. The final output shows the averaged shear wave velocity value from depths of 0-200km. The top 1km contains values for every 0.1km and the top 10km is spaced every 0.25km. Our study is primarily interested in constraining the crust, so we mainly examine the top 30km.

3. Results

3.1 ZH ratios

We obtained ZH ratios primarily between the periods of 5-10s (in 0.5s increments) shown in **Figure 6** for selected stations within each subarray. Each set of colours represents ZH ratio measurement from each pair of directional components (red and blue), which is averaged to obtain the mean (green). The vertical error bars represent the uncertainty in measurement. We note that some stations such as E3H1 only contains measured ZH ratios from one pair of directional components. The data outside the 5-10s period range was found to have too low SNR to allow measurement of ZH ratio.

We marked the locations of the selected stations in **Figure 7a**. In **Figure 6** we observe that the ZH ratios of CU23, GW12, S3B3 and E1D2 are all relatively high since they are above 1. We expect low values to be correlated with the presence of sedimentary structure (Li et al., 2016). For example, S2C1 and E3H1 display ZH ratios below 1 and are located in the Murray and Sydney basins respectively. Note that the right column (E1D2, GW12, S3B3) contains ZH ratios that are relatively stable across all measured periods. The left column (CU23, E3H1, S2C1) differ significantly with increasing period, indicating more lateral heterogeneity at these locations.

We interpolated the measured ZH ratios from each station to produce maps across the periods of 5-10s shown in **Figure 7**. **Figure 7** also shows the station coverage for the ZH ratio measurements for each period. This reveals that some stations are not able to measure ZH ratio for certain periods. Stations that are unable to measure ZH ratios at all feature prominently in the EAL3 array. This is likely due to having too low SNR caused by some problems in the pre-processing step. We found that during extraction from raw data, the EAL3 subarray was missing many records. Despite this, some stations in this array are still functional. Aside from the EAL3 stations, only a few stations could not be measured and include: CU09, E2C1, E2F4, GW14 and S2B9.

ZH ratios are found to be generally high across most of the region and low where it corresponds to sedimentary basins **(Figure 7)**. The location of the Sydney-Gunnedah (north-east) and Murray-Darling (south-west) basins is well indicated by the sharp contrast. In the case of Sydney, most of the contrast is further to the north-west of the main basin. The Murray basin is spread out over a much larger area

and the ZH ratio of this basin is particularly low in the south-west corner. Interestingly, the northern Curnamona province also exhibits consistently low ZH ratios, indicating thick sedimentary cover over this area. In general, we also observe that the low ZH ratios diminish with increasing period while the high values remain stable. This potentially indicates the gradual transition from the sedimentary layer to basement.
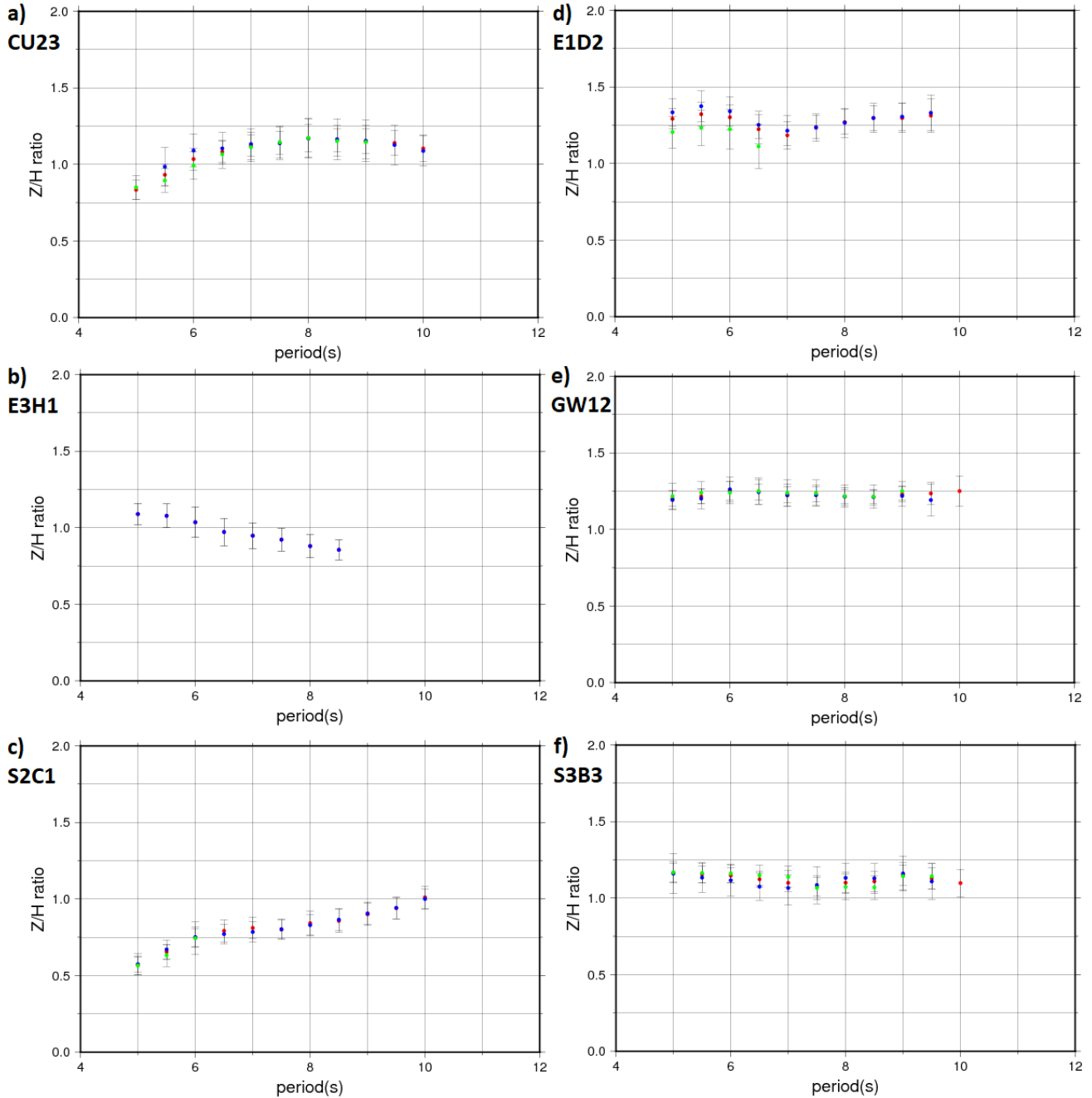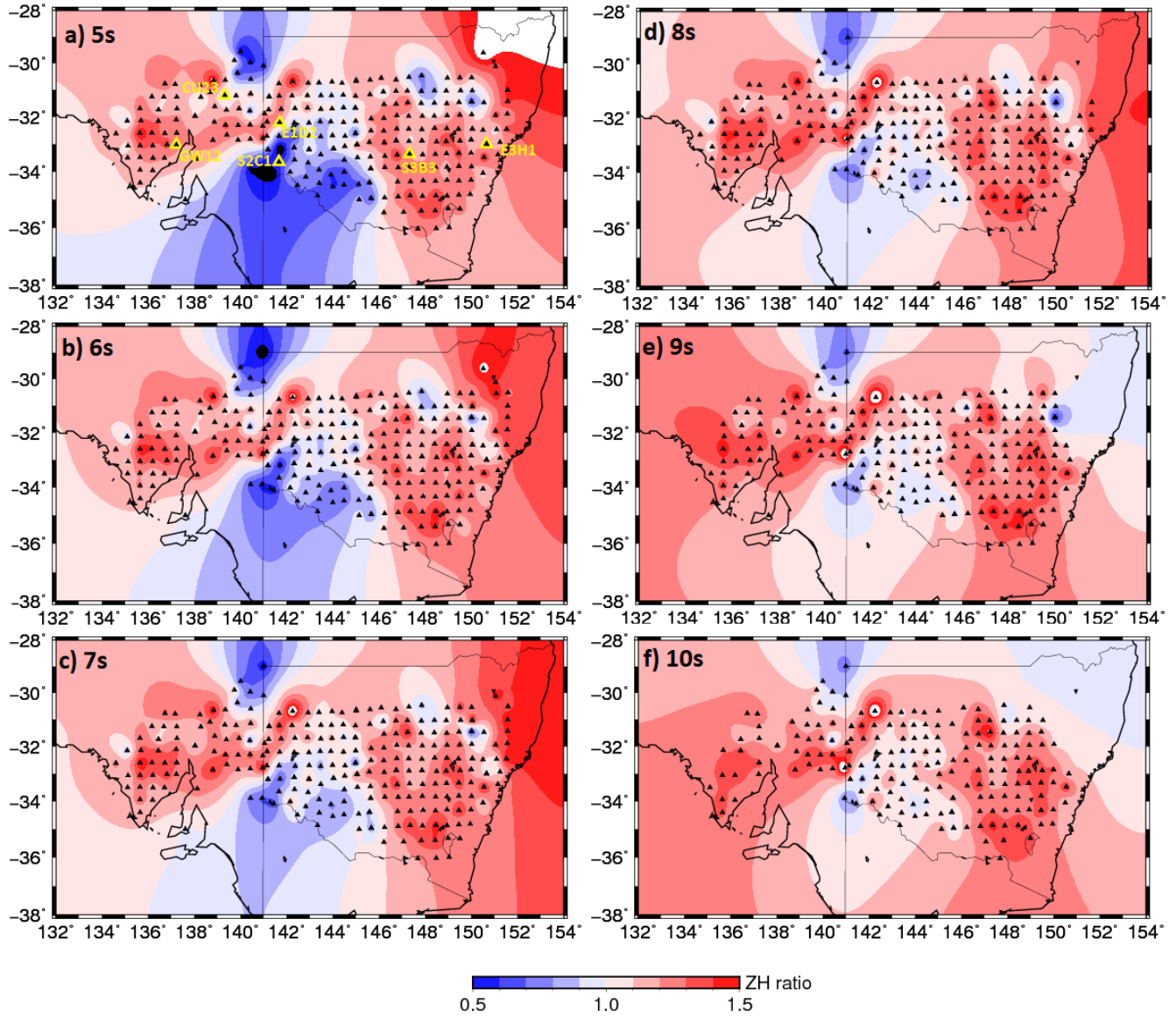
Figure 7: *Interpolated ZH ratio map by periods 5-10*
a) 5s, b) 6s, c) 7s, d) 8s, e) 9s, f) 10s. Triangles indicate the seismic station coverage. Note that the
*EAL3 array (north-east) is missing many stations, especially at 9-10s.*

3.2 Phase Velocity Tomography

Our phase velocity measurements are derived from a 2-D tomographic model which evaluated the SNR of each raypath passing between each station. **Figure 8** shows the plotted raypaths which are selected between the periods of 2-10s. We can clearly observe that 2-8s has strong coverage within each subarray. The greatest overlap in the southern part of the region is found to be between the 5-8s periods. When reaching 10s period however, the number of accepted raypaths begins to diminish rapidly.

Figure 9 shows the results from the phase velocity tomography that was used in the joint inversion**.** The tomography revealed several major structures with a complex geometry, with 7 distinct zones of alternating low velocity and high velocity. Starting with the Western-most Gawler region, we observe higher velocities consistent with the location of the Gawler cration. To the east of this block is a large low-velocity region coinciding with the location of the Murray basin and Delamarian orogen. There is a small high-velocity triangle wedged between these two units, which fits well with the known location of the Curnamona craton. Further east is a long stretch of high velocity zone that indicates the eastern part of the Lachlan orogen. The pronounced high velocity core of this block may be linked to the metamorphic Wagga Omeo complex (139, -36). Finally, a narrow structure extending from the coast in the North-West direction outlines the shape of the Sydney-Gunnedah basin. This is bounded by a small high velocity block in the north, which highlights the transition to the New England Orogen.

As we go deeper into the 8s period, there is a presence of a strongly fast anomaly just south-west of the Gawler craton (138, -35). This area marks the Adelaide Rift Complex, but the margin is difficult to constrain. This anomaly lies outside our data region and only has long raypaths passing through it where the arrays overlap **(Figure 8)**. Due to the lack of longer raypaths, only 3 notable structures are visible when we reach 10s period.
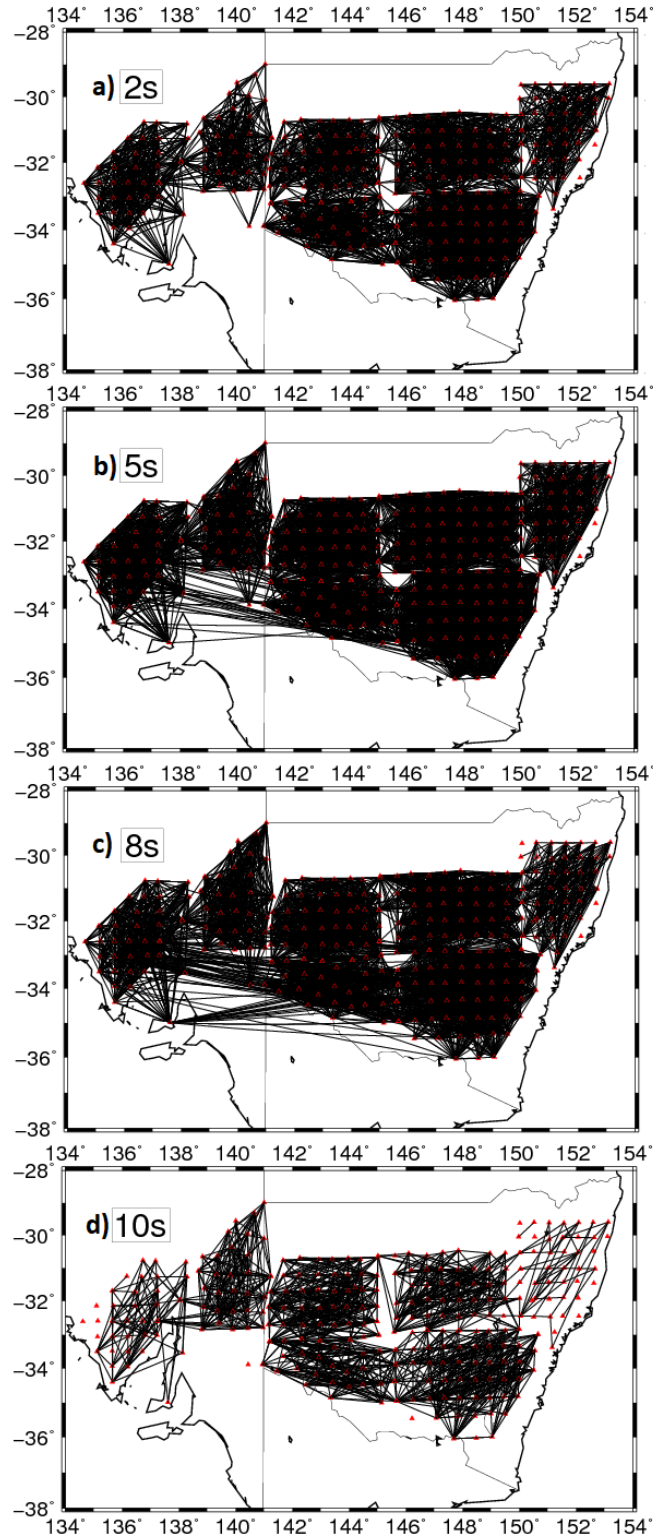
Figure 8: *Phase velocity model – accepted raypaths by period*
*a) 2s, b) 5s, c) 8s, d) 10s*
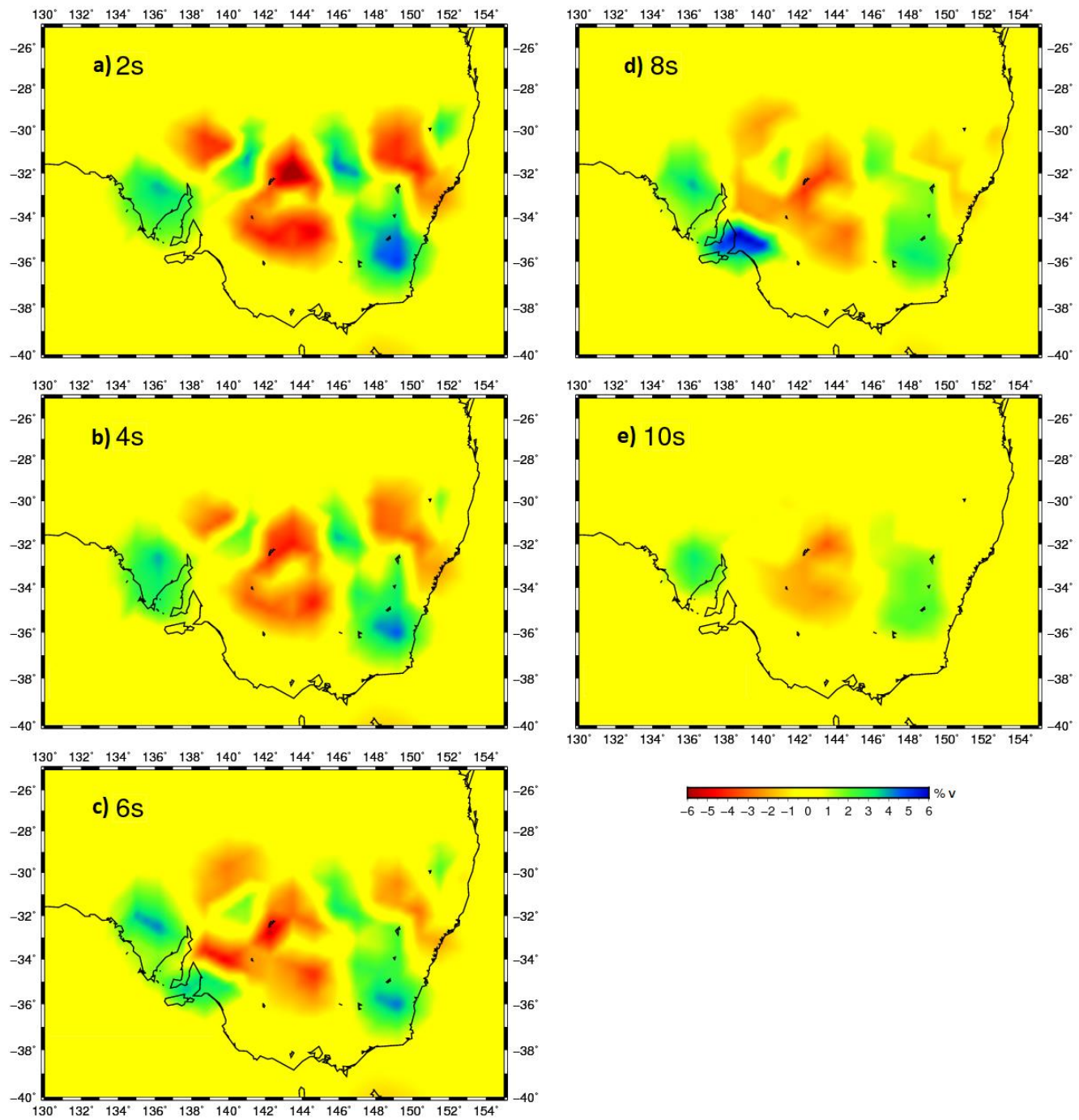
Figure 9: *Output phase velocity perturbation maps by period*
a) *2s, b) 4s, c) 6s d) 8s e) 10s*

3.3 Joint Inversion

3.3.1 1-D Vs models

Our Vs model is made up of a grid of 1-D Vs models, each reflecting the shear velocity structure beneath that point. Examples of the 1-D Vs model are shown in **Figure 10**. From this we created 2D depth slices as well as cross-sections to build a pseudo-3-D model of the South-East Australian crust.

The 1-D Vs models plotted in **Figure 10** belong to 3 different areas of interest. These models are located in the Murray basin (red), Lachlan Orogen (green) and Sydney basin (blue). The general trend of the Vs model is a rapid increase to 3.5km/s between 0-3km followed by a gentle transition into MOHO velocities of around 4km/s. We can observe that the main variations between the models are in starting velocity of the top sedimentary layer and the MOHO transition at 30-40km depth. After 40km there is little variation between the models. Note that the Vs model beneath the sedimentary basins approach high velocities at greater depth than for the Lachlan Orogen.
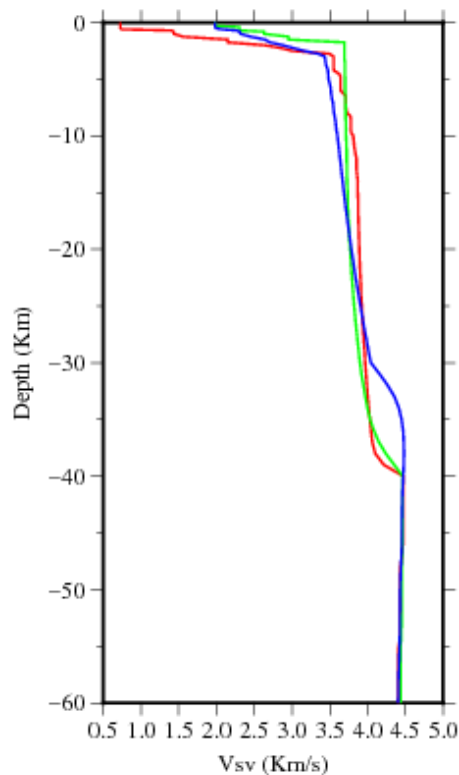
Figure 10: *1-D Vs Models beneath selected locations*
*Red: Murray Basin (141, -34). Green: Lachlan Orogen (149, -35). Blue: Sydney Basin (150, -32).*

28

3.3.2 Depth Slices

The result of our joint inversion is shown in **Figure 11 and 12**, which contain shear velocity depth slices of the study region and the % perturbation of Vs respectively. We apply smoothing to the maps and regions beyond the extent of our array are cut out.

The shallowest layers **Figure 11a-b**, are defined by anomalously slow velocities in the northern Curnamona province and Central Murray basin of south-west NSW. The rest of the Murray basin displays a moderately slow velocity, which matches the velocities beneath Sydney Basin. The highest velocities are observed in the Gawler region, Adelaide Rift Complex and Lachlan Fold Belt. We determined that the low velocities correlate well with locations of sedimentary basins and the high velocities are mostly located in mountainous areas. The reason for the strong anomaly in the northernmost Curnamona is possibly due to the presence of multiple overlapping sedimentary sequences **(Figure 3a)**. There are also some anomalies near the New England Orogen at 2.5km depth, with strongly slow anomalies surrounding a high velocity centre. This may mark the transition from the forearc basin units of the Tamworth belt into the Permian-Mesozoic igneous rocks of the New England Orogen.

At 5-10km **(Figure 12a-b)**, the Sydney basin area in the east strongly defined as a slow anomaly stretching to the north-west as it wraps around the New England Orogen. As we move west, there is a major transition into a large stretch of a faster unit, outlining the Lachlan fold belt. The south-eastern part of this unit is anomalously fast and has the inferred shape of the metamorphic Wagga-Omeo complex. To the west of this is another major slow unit coinciding with the location of the Murray-Darling Basin. Directly below this unit is a high velocity block, bounded by low velocities from all sides. In the north Curnamona province, we see a strongly anomalous high velocity area which continues southward. This is the complete opposite for the 1km and 2.5km layers, which reveal a very slow anomaly possibly due to thick sedimentary cover. We cannot clearly infer the edge of the Curnamona craton at this depth as we would expect a small circular shape around 141, -31. The next slow anomaly to the west of this can be inferred to make up part of the Adelaide fold complex that extends further south. This unit shows a strong transition in the west into what is clearly the Gawler craton, which is a fast structure as expected.

As we go deeper into 15-25km **(Figure 12e-g, Figure 13c-g)**, the boundaries between these units change drastically and the extent of the variation is reduced. The lower velocity anomaly beneath Sydney basin is greatly diminished and becomes a high velocity zone at 25km depth. The low velocities below the Murray basin become less concentrated and spread to cover most of western NSW. From 20km depth and below we observe connectivity between the higher velocity structures beneath the Gawler and Curnamona province. It also appears that the slow western half of the Gawler craton becomes distinct from the faster eastern part at greater depth. At 30km, heterogeneity increases significantly as we begin to approach the MOHO for most areas. In **Figure 11h and 12h**, we observe that the two main areas that have increased velocities due to the MOHO transition are between the Gawler and Curnamona provinces and beneath Sydney Basin in the east.
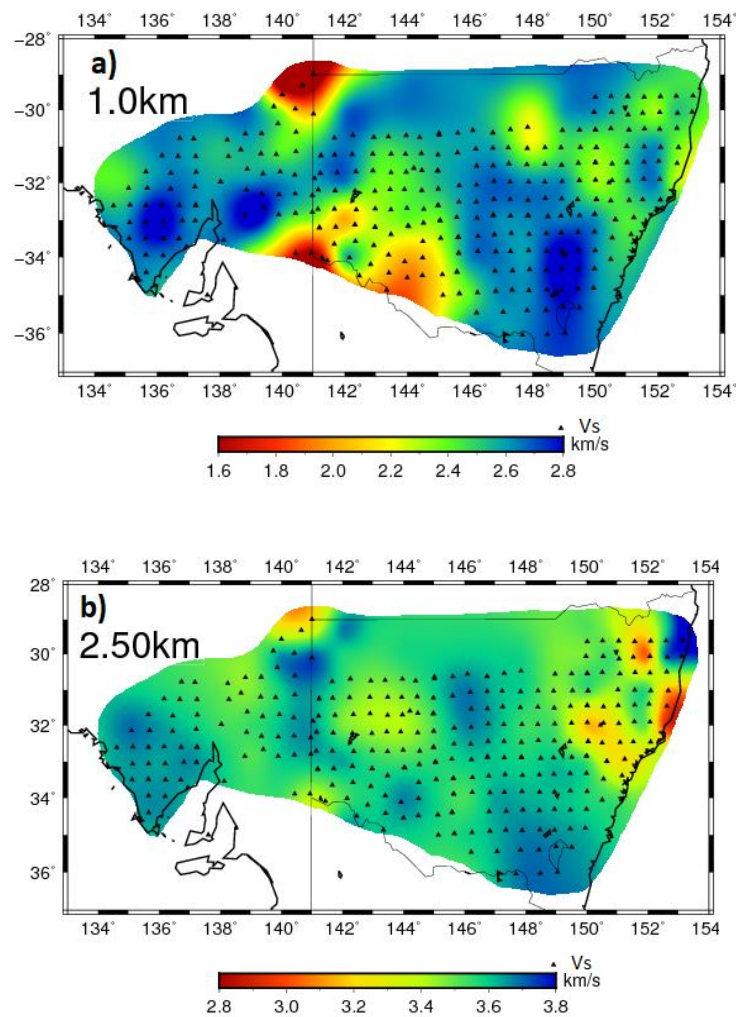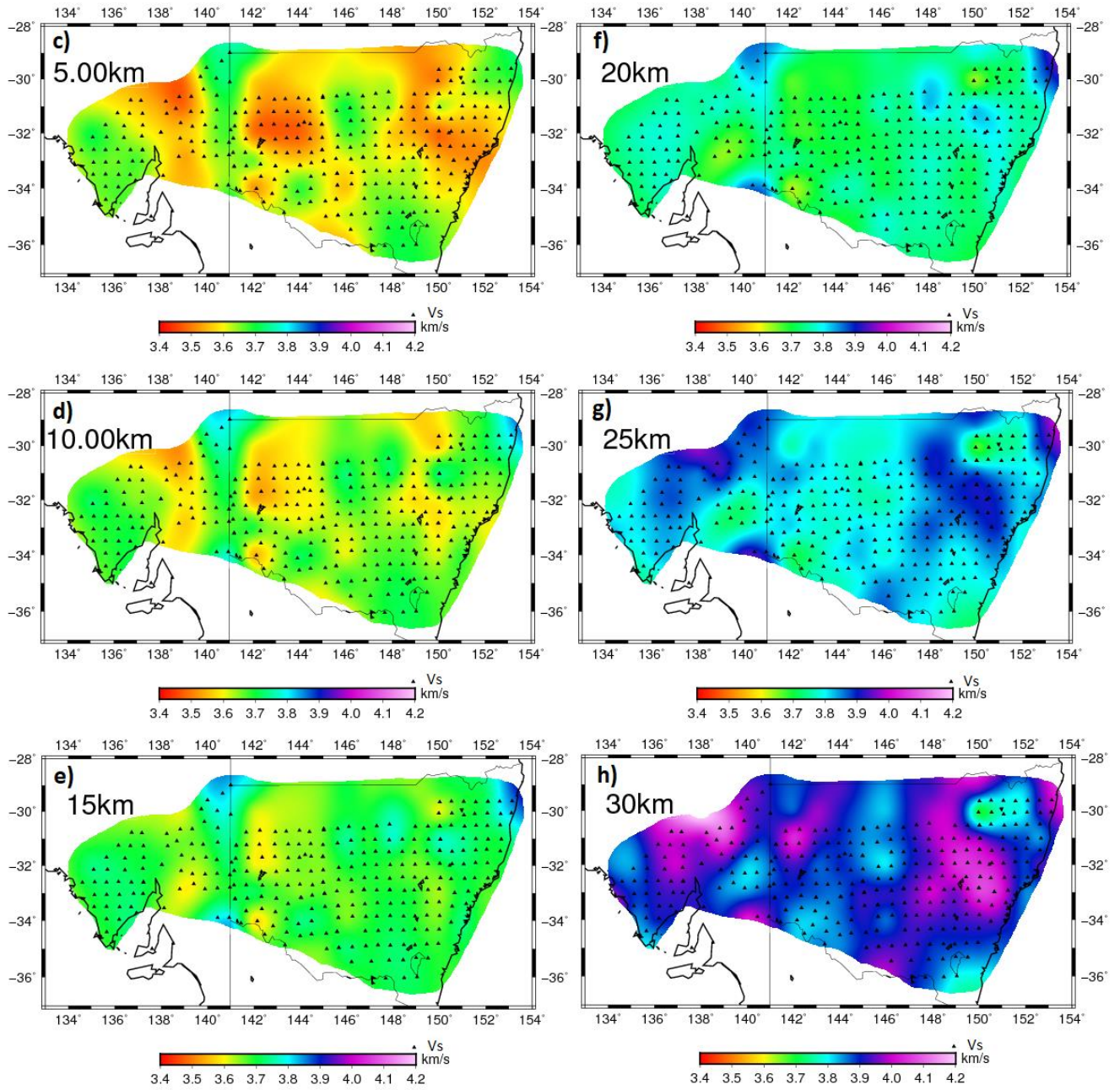
Figure 11: *Vs model depth slices from 1-30km*
a) and b) use a specific scale while c) to h) are plotted with the same scale.
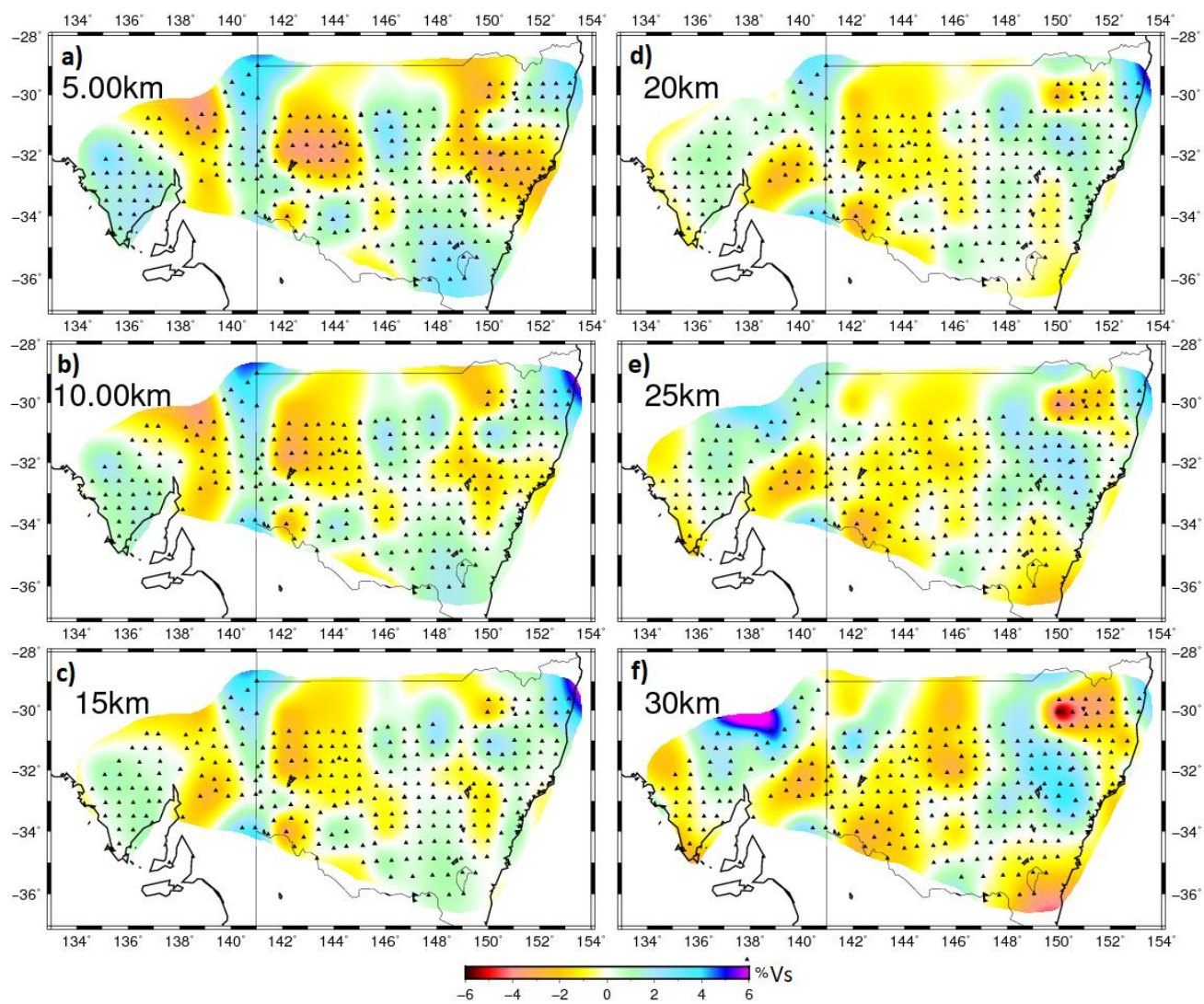
*Figure 12: Vs model percentage perturbation maps for 5-30km
a) 5km, b) 10km, c) 15km, d) 20km, e) 25km, f) 30km*

3.3.3 Cross sections

We plotted cross sections to examine the variations in the topmost sedimentary layer across the study region. **Figure 13** defines the lines that the cross sections are plotted along. Cross sections along the latitudes -31 to -34 (pink) are contained in **Figure 14.** Some additional cross-sections across areas of interest (white) are plotted in **Figure 15**.
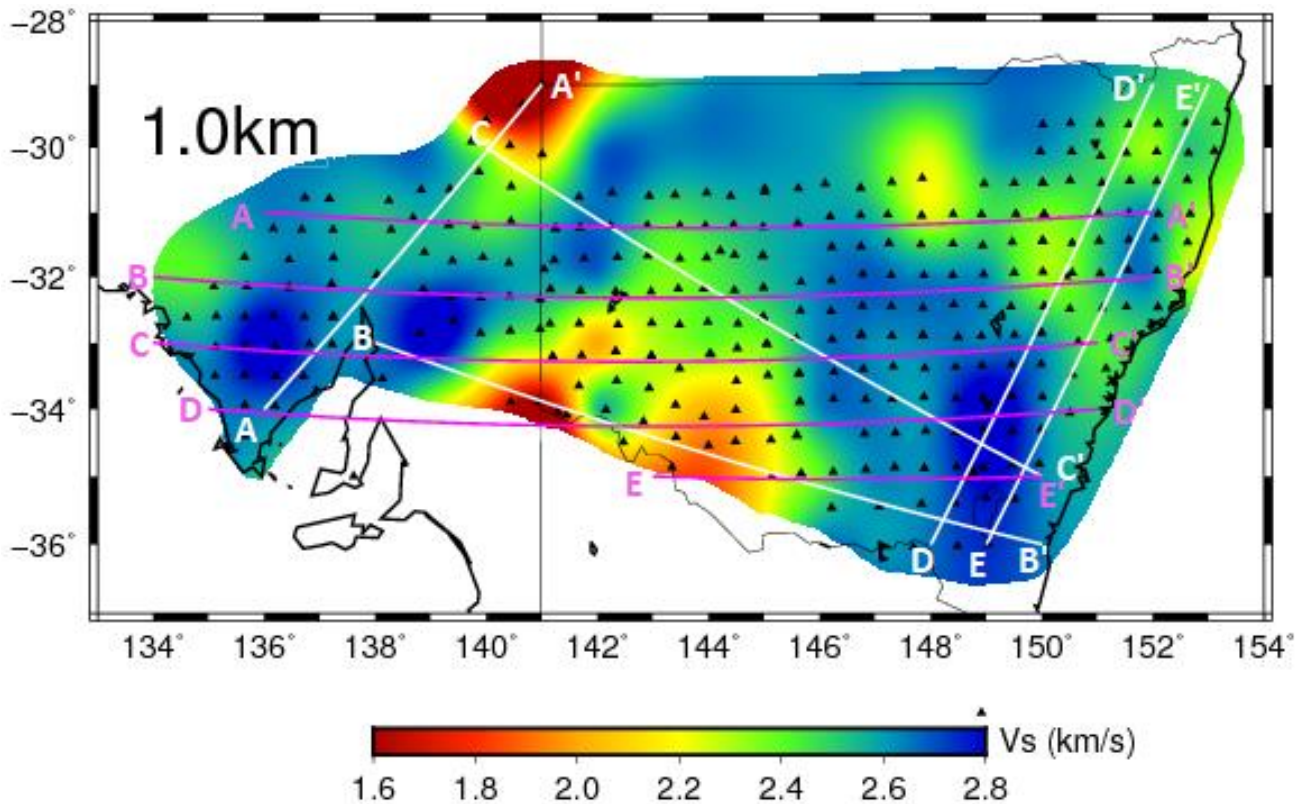
Figure 13: Lines along which cross-sections are plotted
The pink lines are plotted in Figure 14, the white lines refer to Figure 15.

In **Figure 14** we observe a slow, shallow top layer across all latitudes between 0.5-2km thick. This slow layer appears to thicken in areas corresponding with sedimentary basins which contrasts with thinning beneath mountainous topography. The northernmost cross-section (-31) appears to have the most uniformly slow layer compared to more southerly areas. This indicates that the northern part of NSW contains a wider distribution of sedimentary cover. As we proceed further south, there is more contrast between the inland basin area which is bounded by the east coastal Lachlan fold belt and the Adelaide

Fold Belt in the west. This contrast is most visible along the -34 latitude **(Figure 14d)**, where there is clear delineation of two basinal structures between the mountains at 139 and 146 longitudes. These structures are located beneath the Central Murray Basin and appear to extend further north in **Figure 14c**, where they narrow significantly. The south-east corner of NSW shown in **Figure 14e** displays a severely thinned sediment layer beneath the mountains, which nearly doubles in thickness as it approaches the inland basin. This sediment layer exhibits an uncharacteristic flat bottom as it reaches the edge of our dataset.

In **Figure 15**, we chose lines of interest that show significant contrast between key geological units. **15a** displays a thin, flat sedimentary layer beneath the Gawler region, which thickens considerably when approaching the Curnamona province. These are both relatively low-lying regions, though the Gawler is enclosed behind the Adelaide Fold Belt.

In **15b** a strong contrast is observed for the Murray-Darling in the south-west of NSW. There appears to be two distinct, separated structures over a wide, flat plain. As we have gathered from the depth slices, these central basins are not as localized as Sydney basin and are known to be much thinner. This does not seem to be the case as our model shows the depth extent to be nearly 2km in a very concentrated area. Furthermore, the surface velocity starts at a much lower value, in the order of <1km/s, which is almost half that of estimates for other areas.

The profile in **15c** shows a contrast between the thick sediments over Curnamona to the Lachlan Fold Belt in the South-East. The sedimentary layer beneath the Lachlan is considerably thinned, especially at around 149 longitude. We also detect the presence of thicker sediments in the northern part of the Murray Basin, between the two units.

For the Sydney Basin profiles **(15d and 15e)**, we observe a narrow, trough-like structure in a low-lying topography area that is surrounded by mountainous topography. The centre of this structure (latitude 151) lies nearly exactly where the Sydney Basin is located as per **Figure 13.** In the first profile, this basinal feature appears to be dipping to the south-west, into the Lachlan Orogen. As we move more inland, the basin appears narrow and more symmetrical. In addition, the surrounding area along the inner line appears to be more heterogenous.

a) -31
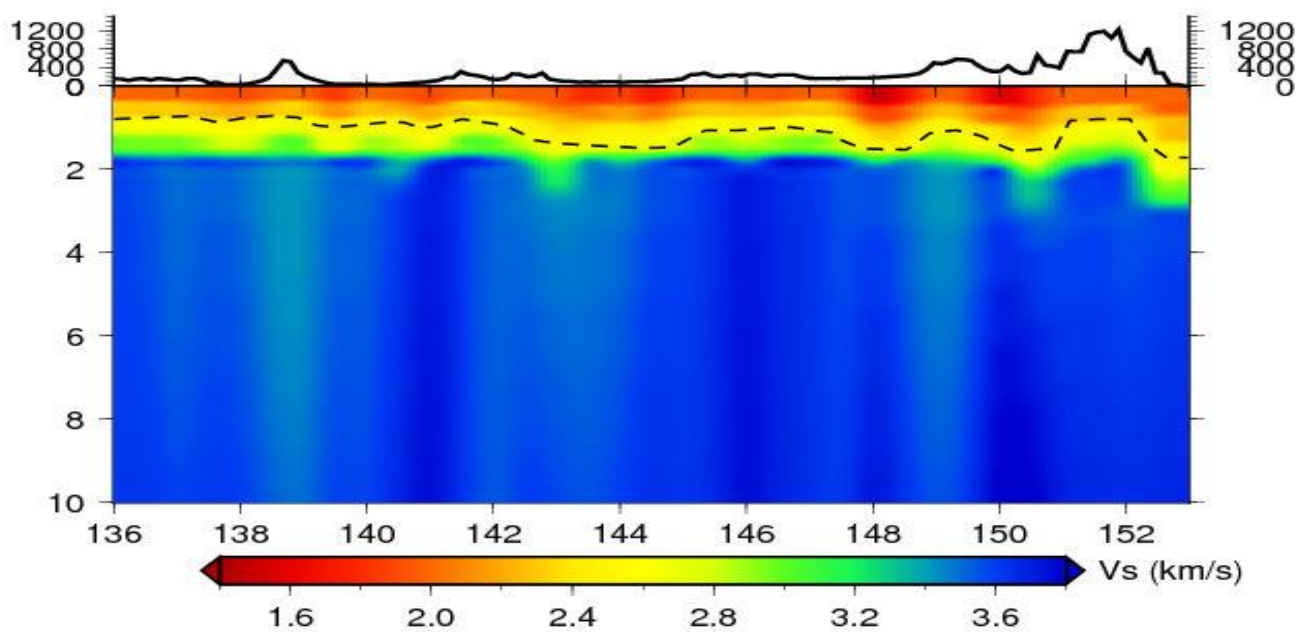
b) -32
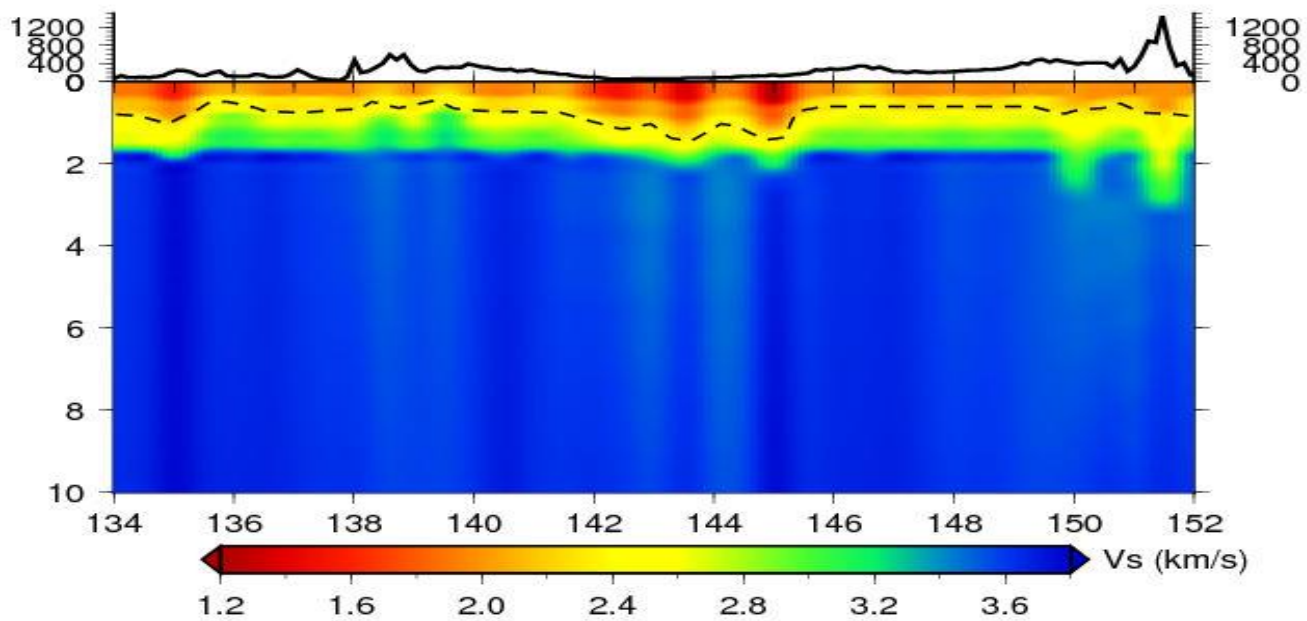
c) -33
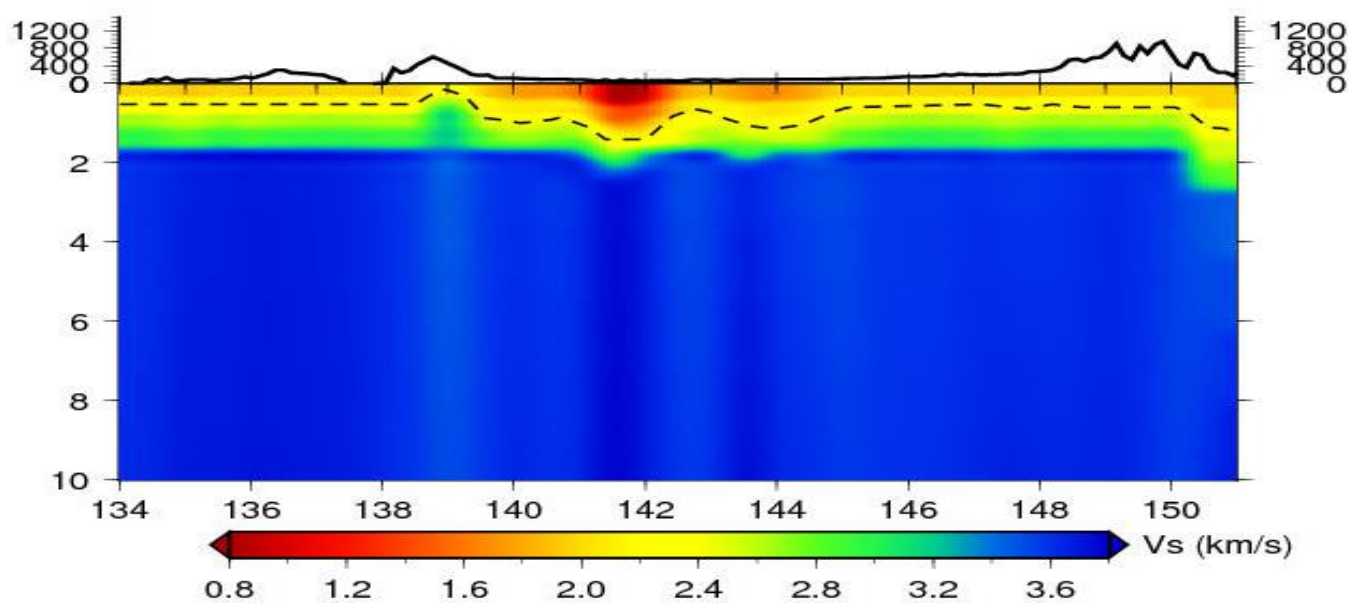
d) -34
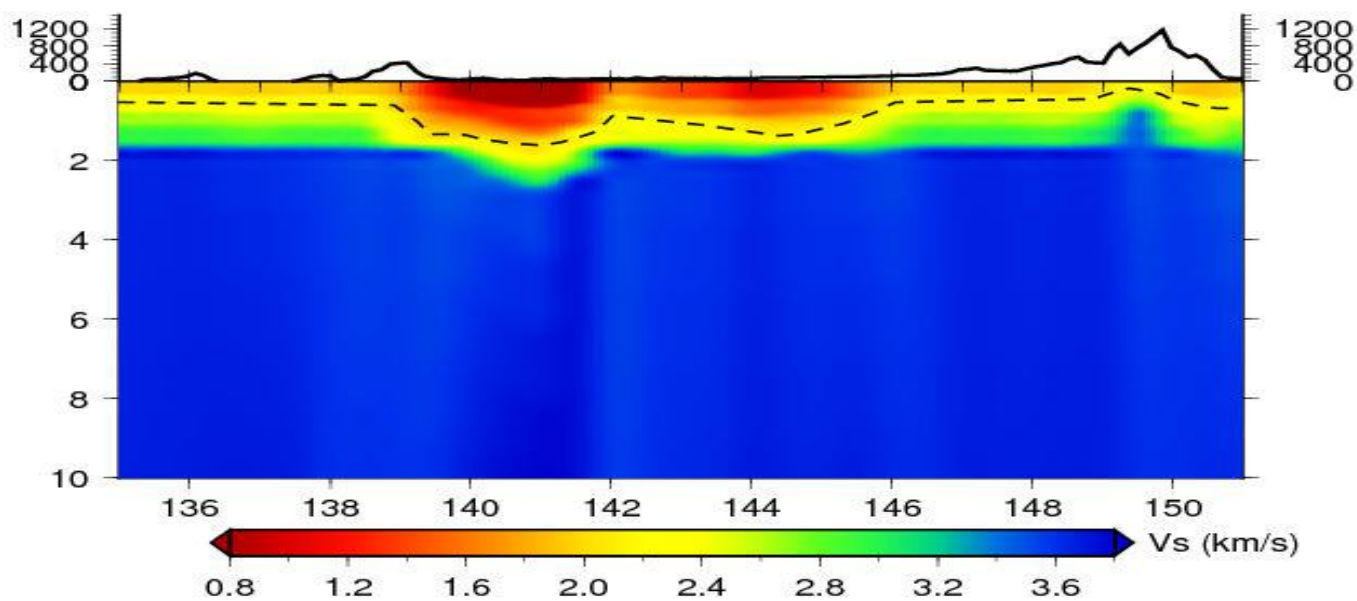
e) -35
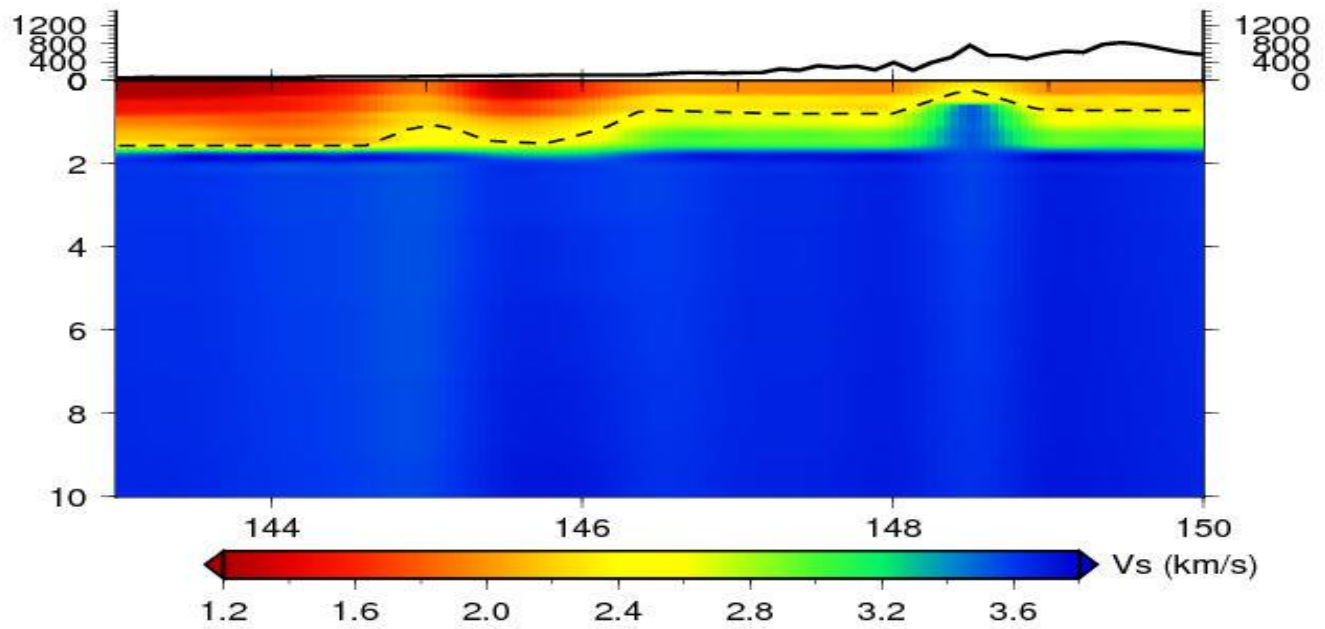
Figure 14: 10km deep cross sections of Vs model along Latitude
a) -31, b) -32, c) -33, d) -34, e) -35. The dashed line represents the interpreted bottom of the sedimentary layer. The plot above shows topography.

a) GW to CU
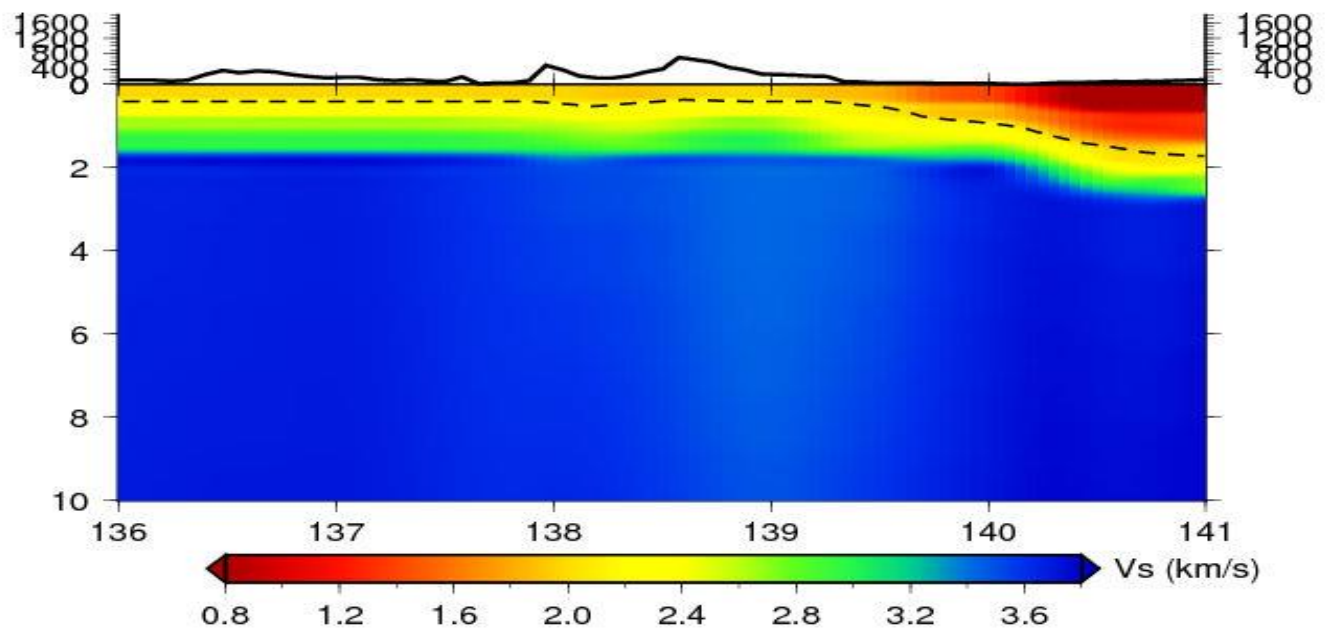
b) Murray
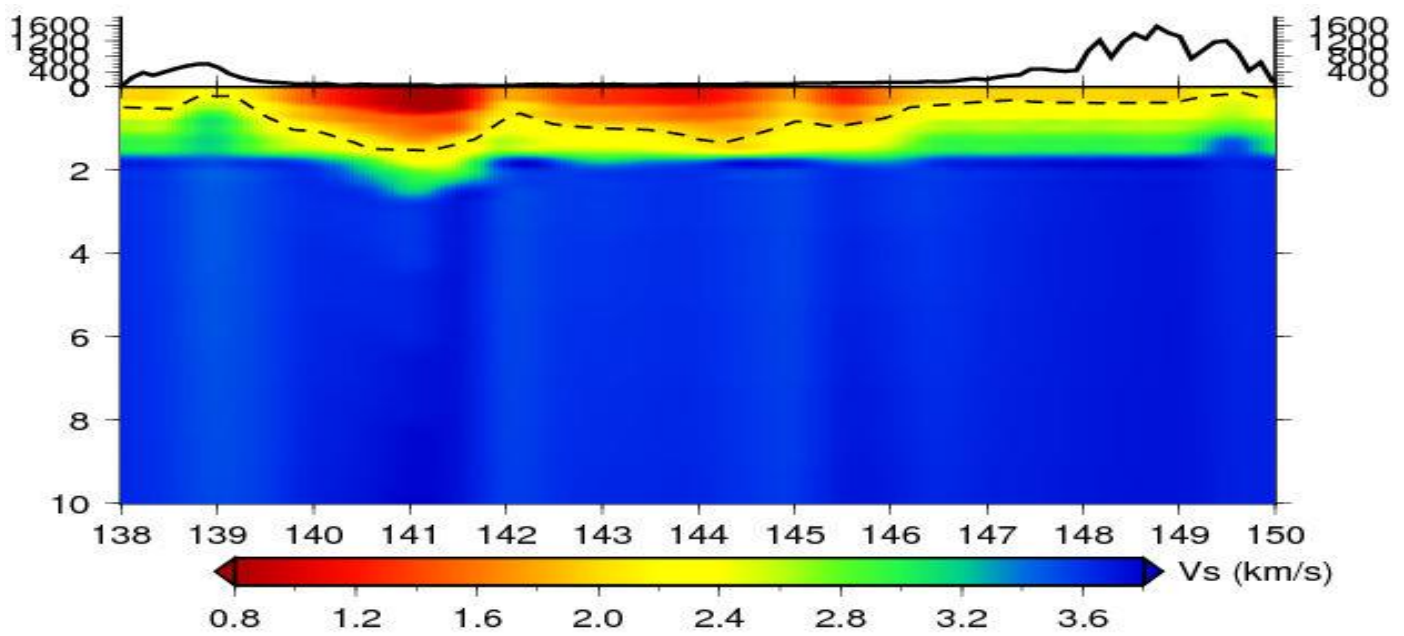
c) CU to SEAL3
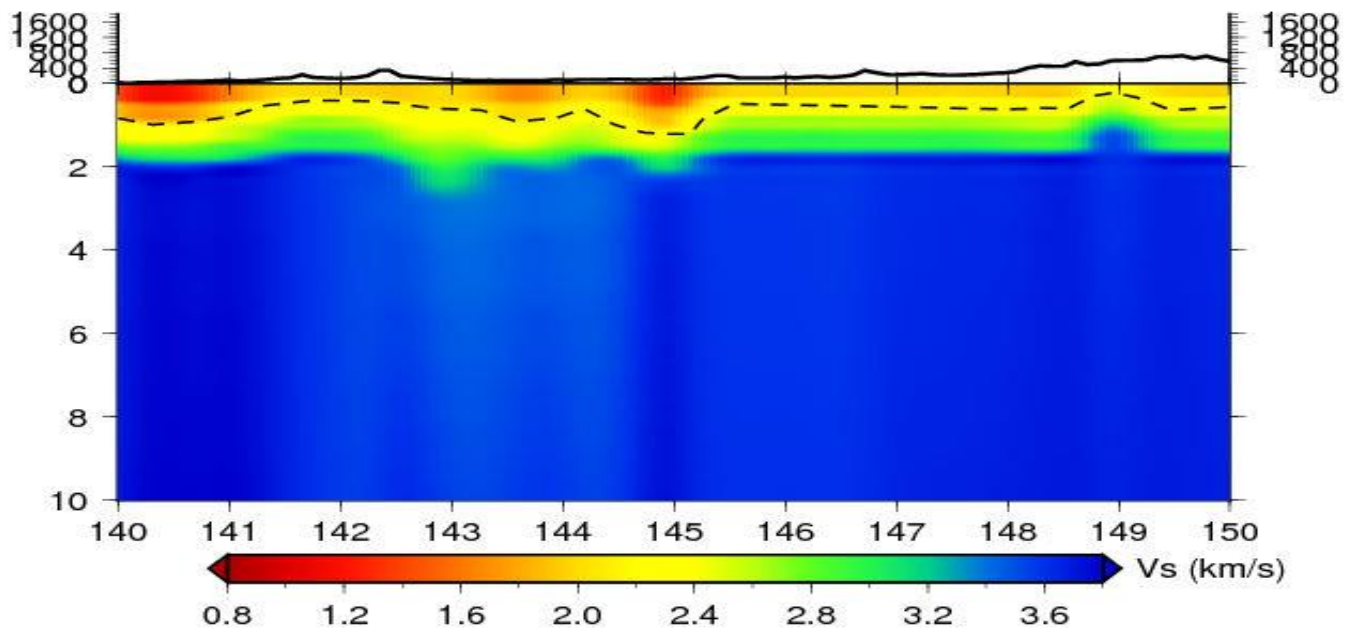
d) Sydney (latitude -36 to -29)
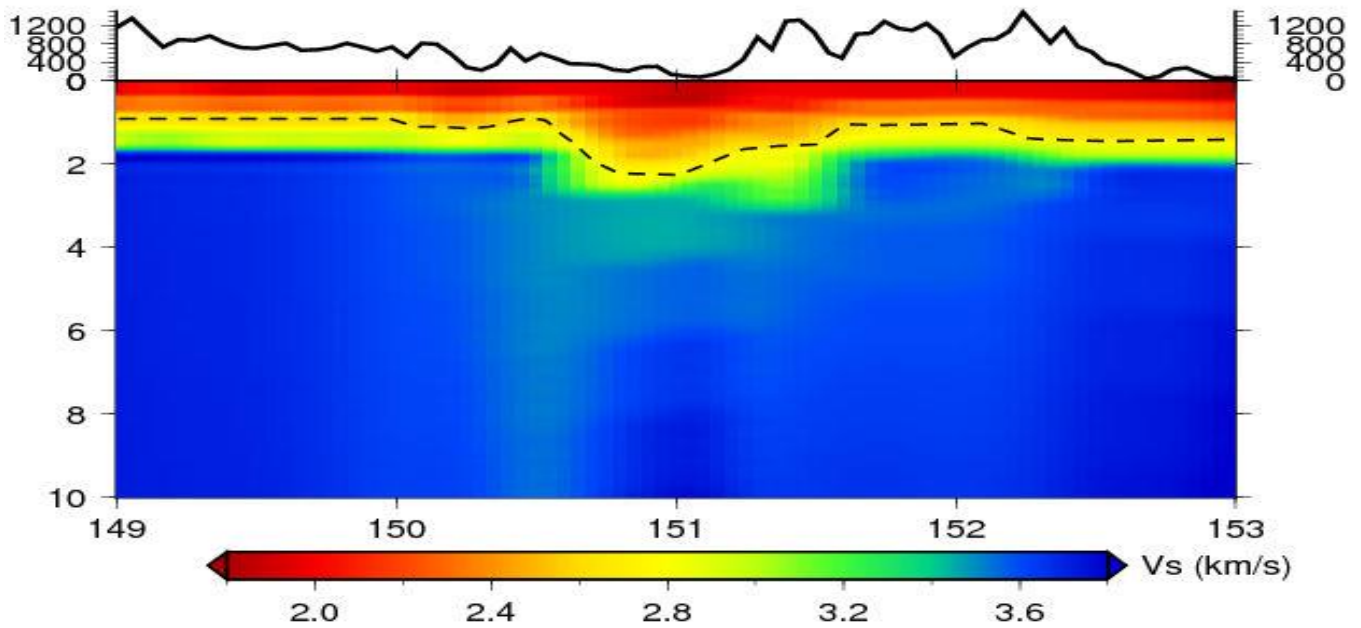
e) Sydney (further inland)
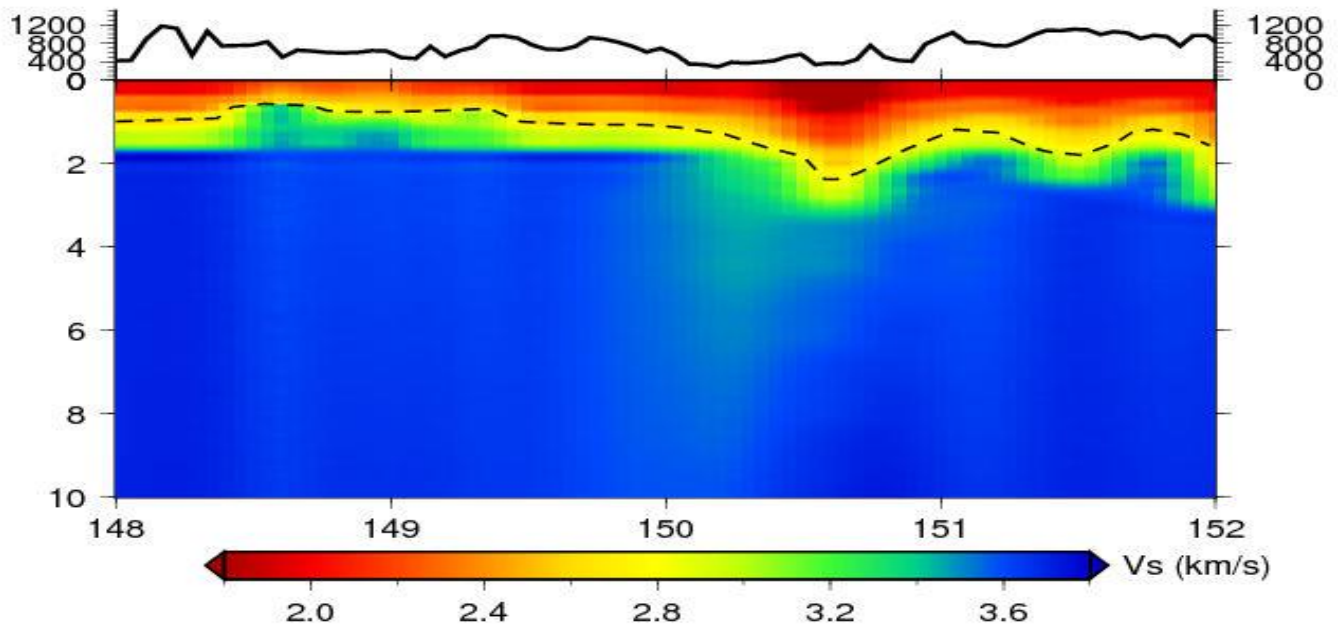
Figure 15: *10km deep cross sections of Vs model across areas of interest defined in* *Figure 13*
*a) GW to CU array, b) Murray basin, c) CU to SEAL3 array, d) and e) Sydney Basin. The plot above the
cross section shows topography*

4. Discussion

4.1 Geological Interpretation

4.1.1 Sedimentary structure

One of the aims in this study is to uncover evidence from tomography that will allow us to make some geological interpretations about the study region. The near-surface sedimentary layer in particular, was predicted to be well constrained due to our use of ZH ratios.

We refer to **Figure 16**, which displays our model at 1km and 5km depth, overlain with geological interpretation from Gray and Foster (2004). The most distinct feature of our model is the low velocities measured in sedimentary basins with extremities in the central Murray (South-west NSW) and Northern Curnamona province. The anomaly in the Curnamona is interpreted to represent thick sedimentary cover from the nearby Mesozoic Eromanga and Paleozoic Arrowie basins **(Figure 3a)**. In addition to this are detectable lows beneath Sydney Basin, which extends to cover most of north-east NSW.

We delineate the presence of two distinct basin structures in the Central Murray in **Figure 15b**, approximately 1.5km deep. The western part of the Murray appears to be deeper and narrower than the adjacent basin. This is evidence for the Murray basin experiencing subsidence in Tertiary, where it's drainage pattern was diverted to the west (Ollier, 1995). Given that the Murray cover sequence is known to be relatively thin (~400m), these steep structures reflect older underlying infrabasin sequences (Brown and Stephenson, 1991). While not as distinct near the surface, the northern part of the basin shows consistently lower velocities at depths below 5km **(Figure 16b)**, which is indicative of the underlying Darling basin sequences.

The near-surface structure beneath Sydney Basin is not as strongly defined but this region still shows some contrast with its surroundings **(Figure 16a)**. In **Figure 15d-e,** we observe a 2km deep, south-west dipping structure beneath the Sydney Basin, which is far shallower than predicted. The consistently lower velocities beneath the Sydney Basin area at 5km and below, lead us to believe that there is a continuation of sedimentary sequences until at least 10km **(Figure 12)**. This indicates that the anomalies we detected in the top 2km represents a more unconsolidated surface layer.
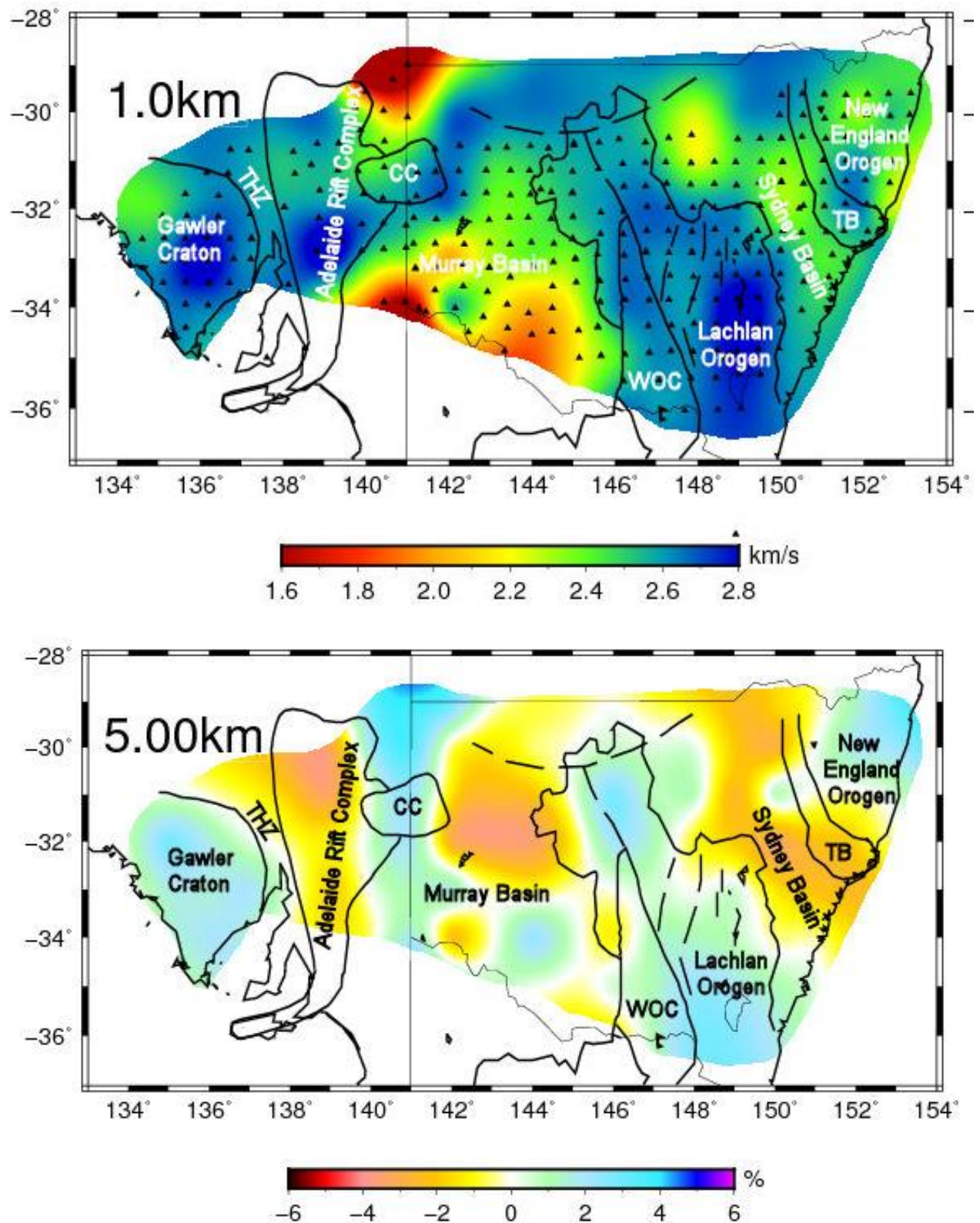
Figure 16: *Surface geology overlain over a) Absolute Vs map at 1km b) Vs perturbation at 5km. From Gray and Foster (2004). THZ=Torrens Hinge Zone, CC=Curnamona Craton, WOC=Wagga-Omeo Complex, TB=Tamworth Belt*

4.1.2 Crustal structures and boundaries

Continental accretion involves the gradual accumulation of exotic crustal material over complex tectonic cycles of convergence and extension (Moresi et al., 2014). As such, the accretionary orogens should contain a complex assemblage of continental fragments and faults that can be distinguished in our model. This is supported by previous seismic tomography studies that revealed evidence for micro-continent structures further south of our study region (Pilia et al., 2015). As we go deeper in our model, finer structures are revealed beneath the Murray basin, which belong to the underlying Lachlan orogen. We overlay our interpretation of boundaries for known units and faults in **Figure 17a** for the 5km depth. **Figure 17b** serves to display the clear demarcation of the Bootheragandra fault at 20km depth.
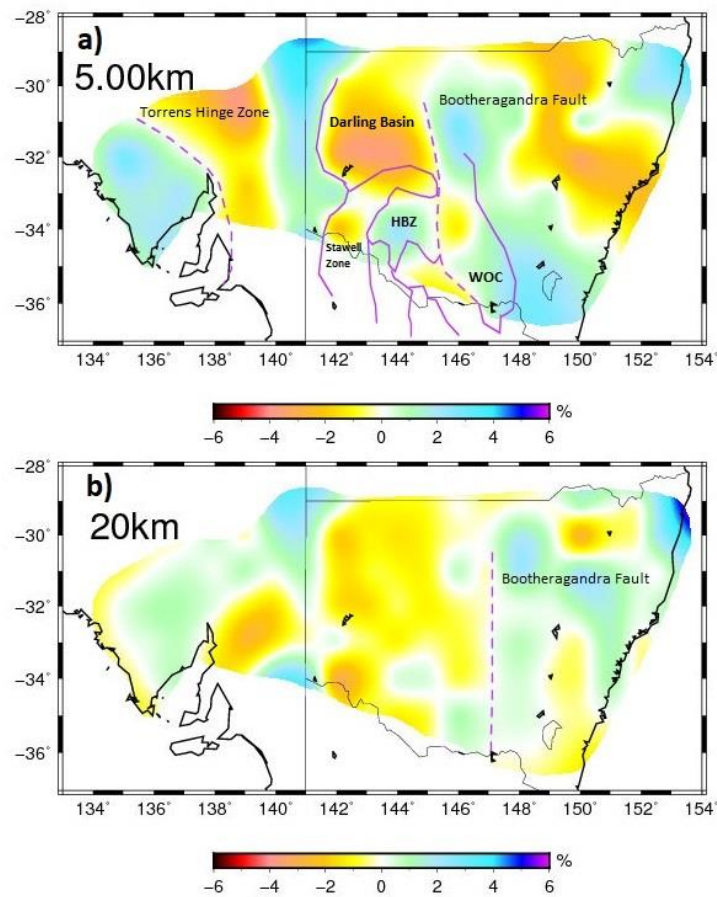
Figure 17: Interpreted tectonic units and faults of the Lachlan Orogen beneath the Murray Basin at a) 5km, b) 20km. The solid lines represent interpreted tectonic units. Dashed lines are inferred faults. HBZ=Hay-Booligal Zone, WOC=Wagga Omeo Complex. Adapted from Pilia et al. (2015), Glen et al. (2013), Young et al. (2013).

At 5km, we observe a higher velocity block which is bounded at all sides by low velocities. We interpret this to be the Hay-Booligal zone, a basement unit containing Silurian-Devonian granites and volcanics (Glen et al., 2013). The zone is well imaged by Magnetic studies, which infer a suture zone of S-type granites along the western border, with the eastern border bounded by the Bootheragandra fault (Carlton, 2010). This fault is well documented in other seismic models (Young et al., 2013, Pilia et al., 2015), and is also clearly visible at 20km depth **(Figure 17b)**. The Stawell zone also borders the Hay-booligal unit to the east, which we interpret to have some connectivity to a structure beneath the Darling Basin unit.

Of key interest to seismic studies in this region is the location of the transitory Tasman line, that marks the boundary from Phanerozoic to Precambrian units in the west (Rawlinson et al., 2014). In our model, we interpret this to be along the clearly defined Torrens Hinge Zone in **Figure 17a**. The boundary between Delamarian and Lachlan orogens is interpreted to be along the west margin of the Darling Basin and Stawell Zone. This is presumed to continue south and align with the Moyston fault in Victoria (Glen, 2013).

As we approach 20km depth **(Figure 17b)**, these boundaries are not as clear. The observed connectivity between the Gawler and Curnamona province could be evidence of their sharing of the same crust prior to the Neoproterozoic (Pilia et al., 2013). The model of Young et al. (2013) favoured an extensional regime to explain the formation of the Torrens hinge zone. This is because they found it to be associated with a steep-sided rift structure at 23km depth. We do not find a similar structure and in fact the western structures are poorly defined in our model. We attribute this to a lack of resolution at these depths.

4.2 Evaluation

One of our primary aims is to evaluate the effectiveness of using ZH ratios to constrain the shallow sedimentary layer. Our results show that the technique is effective at delineating the presence of near-surface sediments when compared to known surface geology. We are also able to recover some deeper crustal features from our model. In this section, we will compare our results with relevant datasets and studies to point out the strengths and limitations of our model.

4.2.1 Depth constraints

Using ZH ratios to constrain the near-surface layer, we had hoped to obtain accurate estimates of sedimentary basin depth. In our latitudinal cross-sections **(Figure 14)**, what we interpret to be the sedimentary layer does not vary in thickness greatly across the entire region, being roughly 1.5km on average. We interpret the major transition to the basement to be at shear velocities of around 2.5 to 3.0km/s.

When we compare our results to Li et al. (2016) we notice that our sedimentary basins are not as well defined in terms of depth. Li et al. (2016) obtained depth estimates of up to 6km in the northern Songliao basin, which heavily contrasted with the surrounding mountain ranges. In their model, shear velocities <2.6km/s persisted to 3-6km depth beneath the basins, and velocities around 3.0km/s were observed at the surface directly beneath mountains. While their geological setting differs from ours, we still anticipated far greater depth extent in our model, especially since studies report 5-9km depths for the Sydney Basin (Danis et al., 2011).

The presence of a widespread 1-2km sedimentary layer may not be entirely inconsistent with known surface geology. It is known that a majority of the study region is covered in Cenozoic sedimentary sequences that masks the major orogens (Rawlinson and Fishwick, 2012). The model of (Young et al., 2013) also detected a near-surface block of low velocity material which in some areas would thicken to ~10km depth. They interpreted this to reflect the presence of deep, sediment-filled, basin structures. Furthermore, the structures they observed contained shear velocities in the order of 3.6km/s while we can observe much slower material at shallow depth.

The reason our model lacks abrupt variation in the sedimentary layer is likely due to our dataset and the parameterization of our model. In our inversion, we defined a specified Vs range for the top and

44

bottom of the sedimentary layer, all within a depth range of 1.5-3.5km. As such, our sedimentary layer thickness may be inaccurate but strong variations in shear velocity corresponding to thick sediments are still detectable. For example, in **Figure 15c**, severely low shear velocities of almost 1km/s are detected beneath the southern Murray Basin. This demonstrates that our model can improve resolution of the shallow layer but the depth extent of this structure is not always well resolved.

Another important issue raised by Ma et al. (2016) is that basement depth controls the cut-off period of the first higher mode, which coincides with a rapid increase in ellipticity of the fundamental mode. They highlight that misidentifying the higher mode as fundamental in the inversion leads to anomalously high shear wave velocity. This factor could explain our inaccurate estimates of basement depth, which are shallower than expected. This result emphasises the importance of careful processing to retrieve an accurate shear velocity model.

4.2.2 Data limitations

We experienced some limitations with our ambient noise dataset which meant we were only able to recover short period measurements for both phase velocities and ZH ratio. This may explain the difficulty in recovering the full depth extent of basins and the lack of resolution at greater depths.

In **Figure 5** and **Figure 8**, we showed that we are unable to obtain adequate phase velocity measurements for periods >10s. Young et al. (2013), who used a similar dataset, reported that their greatest model complexity was in the 3-12s period range. For periods >12s they explained that there were higher noise estimates and a decrease in raypath coverage. In the short periods, there was likely to be more self-noise at the short period sensors and additional near-surface effects such as wave scattering and multipathing. These effects make it difficult to rely on phase velocity measurements at the very short periods, which should be considered when interpreting our model.

Additionally, we are only able to retrieve ZH ratios within a narrow band of 5-10s, due to low SNR of the cross-correlations outside this range. Other ZH ratio studies have used much more broadband data. Li et al. (2016) for example, measured ZH ratios between 8-25s from ambient noise and 25-40s from earthquake data, which is far more than we had available. The earthquake dataset was found to be almost as effective as the ambient noise. Considering this, it is possible that earthquake data can supplement the lack of long period information. Seismicity in Australia is limited due to its intraplate

setting but previous studies have used regions of high intraplate seismicity to do tomography (Pilia et al., 2013).

The problems we describe here are mainly due to the array we used, with our dataset confined to only multicomponent stations in the WOMBAT array. Our array only contained interstation paths enclosed within each subarray with little overlap. This meant we could not retrieve many longer period raypaths. The far-field approximation was not adequately satisfied from 10s and onwards resulting in reduced SNR. i.e. The interstation spacing within each subarray could not satisfy the requirement of being at least 3 wavelengths apart (Bensen et al., 2007). As we can observe in the raypath map (**Figure 8**), only the longest raypaths are selected for the 10s period, followed by a subsequent steep drop in acceptable phase velocity measurements **(Figure 5).**

The lack of long period data may have limited our constraints on deeper features. If we refer back to **Figure 1**, we note that the sensitivity of ZH ratio at 8s is only for the top 5km layer with a peak at around 1-2km. At 40s, the sensitivity extends to nearly 20s. Given that we only measured ZH ratios between 5-10s, we likely only sampled the top 5-6km at most. The ZH ratio method is supposed to work best when only considering longer period data, since this means shallow structure can be resolved without needing short period data (Li et al., 2016). Short period data is normally difficult to obtain since it requires an array with very tight station spacing. It also has many associated problems that add noise such as being more prone to scattering effects (Young et al., 2013).

4.2.3 Model limitations

The interpretations we make in seismic tomography are primarily through the lens of fast and slow seismic velocities. In reality, this can reflect multiple different physical properties of the Earth and is not limited to composition alone. In fact, this relationship is highly non-unique and presents a great challenge when making inferences about geological structure (Rawlinson et al., 2014). There are other factors to consider that are controlled by the modelling process. For example, our model assumes an isotropic medium which is generally not the case for the Australian crust (Debayle et al., 2005). Therefore, the outcome of our model, particularly the absolute measured values, are not a perfect reflection of reality as they are heavily controlled by our defined parameters and constraints. We can

assume however, that the relative differences in the measurements is the key to making observations that may reflect a real-world structure.

We found that some of the parameters are not well selected for certain locations compared to others. For example, our choice of sedimentary thickness range (1.5-3.5$m0$) may have limited our ability to observe variations in sedimentary thicknesses. Owing to the limited scope of our study, we neglected to use an appropriate reference velocity model for the Australian crust. This needs to be corrected if we wish to create a more accurate and comprehensive model of the lower crust and upper mantle. Additionally, the MOHO depth range we selected did not encompass the entire range in the study region (Kennet et al 2011). However, if the parameters are allowed to vary too greatly, the models may become more prone to error. Therefore, future studies should choose parameters more carefully while allowing them to vary when inverting for each location.

4.2.4 Summary

We determine that the ZH ratio is highly effective in delineating the extent of near-surface sedimentary structures. While our model shows excellent correlation with surface geology, the basement depth of sedimentary basins is likely to be underestimated. Some deeper crustal structures could be inferred but our model lacks resolution past mid-crustal depths. We have shown that the limitations lie mainly in the lack of high quality, broadband, multicomponent seismic data. In addition, constraints could be improved by more careful parameterization of the joint inversion process.

4.3 Future Work

In the previous section, we evaluated our model and highlighted its main limitations. This has been a useful preliminary study to identify problematic areas that require more focus and review. Here, we will detail the possible solutions which could be adapted in future projects in Australia using ZH ratios.

We showed that there was a lack of ZH ratio measurements in the available period range due to low SNR. Therefore, we need better methods to measure more robust ZH ratio values. For example, Workman et al. (2017) has developed a new single station method to measure Rayleigh wave ellipticity using Frequency Dependent Polarization Analysis. This method has advantages in determining the dominant wave-type in the ambient noise and is also applicable to areas where a dense array cannot be deployed.

The main improvement that would solve many of our data limitations is the deployment of a larger, multicomponent, broadband seismic array. Additionally, greater coverage of other parts of Australia will allow us to infer more geological connections with other parts of the Tasmanides. Of course, this has the greatest associated costs and would not see implementation in the immediate future. A more likely project would involve utilising the existing arrays to their fullest potential. This would include more careful selection of seismic stations in the processing step to extract the least noisy cross-correlations. Adopting the ZH ratio method has meant sacrificing wider station coverage and this has made it difficult to gain constraints on deeper structure. While we succeeded in retrieving a model of shallow crustal structure, a more comprehensive model that links to the upper mantle is needed.

Another possible implementation to solve the lack of long periods is by incorporating Earthquake data, which was the method used by Li et al. (2016), Lin et al. (2014). Suitable earthquake data in Australia is mainly confined to regions of high intraplate seismicity (Pilia et al., 2013), so this may limit the potential study area. Workman et al. (2017) found that while we can assume Rayleigh waves to be the dominant wave-type up to 8s, above this period other wave-types (Love, body and tilt waves) have a potentially contaminating effect on the ZH ratios. A future study should examine this effect when using ZH ratios derived from longer periods.

5. Conclusions

We have obtained the first 3-D Vs model of Southeast Australia that was derived from the joint inversion of Rayleigh wave ZH ratio and dispersion, thus achieving one of our primary aims. Our model shows good correlation with the major tectonic units in South-East Australia. Key geological units such as Sydney Basin, Lachlan Fold Belt, Gawler Craton and Murray Basin are well resolved especially for the upper crust and sedimentary layer. We successfully show distinct low Vs structures in the form of a thickened uppermost layer, which are well correlated with known locations of the Central Murray, Eromanga and Sydney Basins. We also interpret the locations of some mid-crustal units including the Hay-Booligal Zone and Bootheragandra Fault, which achieves our second aim.

To achieve our third aim, we evaluate the effectiveness of ZH ratios to be strong for delineating the locations of surface sedimentary features. However, there are still limitations of our model which mean that we cannot determine large depth to basement variations and deeper crustal features. The cause of these problems lies primarily in the lack of broadband, multicomponent seismic data. We have proposed some suggestions for improvement in future studies which includes supplementing longer periods with Earthquake data or expansion of the existing seismic array.

References

ARROUCAU, P., RAWLINSON, N. & SAMBRIDGE, M. 2010. New insight into Cainozoic sedimentary basins and Palaeozoic suture zones in southeast Australia from ambient noise surface wave tomography. *Geophysical Research Letters,* 37.

BARMIN, M. P., RITZWOLLER, M. H. & LEVSHIN, A. L. 2001. A fast and reliable method for surface wave tomography. *Pure and Applied Geophysics,* 158**,** 1351-1375.

BENSEN, G. D., RITZWOLLER, M. H., BARMIN, M. P., LEVSHIN, A. L., LIN, F., MOSCHETTI, M. P., SHAPIRO, N. M. & YANG, Y. 2007. Processing seismic ambient noise data to obtain reliable broad-band surface wave dispersion measurements. *Geophysical Journal International,* 169**,** 1239-1260.

BODIN, T., SAMBRIDGE, M., TKALCIC, H., ARROUCAU, P., GALLAGHER, K. & RAWLINSON, N. 2012. Transdimensional inversion of receiver functions and surface wave dispersion. *Journal of Geophysical Research-Solid Earth,* 117.

BOORE, D. M. & TOKSOZ, M. N. 1969. Rayleigh Wave Particle Motion and Crustal Structure. *Bulletin of the Seismological Society of America,* 59**,** 331-346.

BROWN, C. M. & STEPHENSON, A. E. 1991. *Geology of the Murray Basin, southeastern Australia*, Australian Govt. Pub. Service.

CARLTON, A. 2010. The latest geological/geophysical interpretation of the NSW Murray Basin basement. *ASEG Extended Abstracts,* 2010**,** 1-4.

CHONG, J., NI, S. & ZHAO, L. 2014. Joint Inversion of Crustal Structure with the Rayleigh Wave Phase Velocity Dispersion and the ZH Ratio. *Pure and Applied Geophysics,* 172**,** 2585-2600.

CONOR, C. H. H. & PREISS, W. V. 2008. Understanding the 1720-1640 Ma Palaeoproterozoic Willyama Supergroup, Curnamona Province, Southeastern Australia: Implications for tectonics, basin evolution and ore genesis. *Precambrian Research,* 166**,** 297-317.

DANIS, C., O'NEILL, C., LACKIE, M., TWIGG, L. & DANIS, A. 2011. Deep 3D structure of the Sydney Basin using gravity modelling. *Australian Journal of Earth Sciences,* 58**,** 517-542.

DEBAYLE, E., KENNETT, B. & PRIESTLEY, K. 2005. Global azimuthal seismic anisotropy and the unique plate-motion deformation of Australia. *Nature,* 433**,** 509-512.

DZIEWONSKI, A. M. & ANDERSON, D. L. 1981. Preliminary Reference Earth Model. *Physics of the Earth and Planetary Interiors,* 25**,** 297-356.

FODEN, J., ELBURG, M. A., DOUGHERTY-PAGE, J. & BURTT, A. 2006. The timing and duration of the Delamerian orogeny: Correlation with the Ross Orogen and implications for Gondwana assembly. *Journal of Geology,* 114**,** 189-210.

FOSTER, D. A. & GRAY, D. R. 2000. Evolution and structure of the Lachlan Fold Belt (Orogen) of eastern Australia. *Annual Review of Earth and Planetary Sciences,* 28**,** 47-80.

GEOSCIENCE_AUSTRALIA 2012. Distribution of onshore sedimentary basins. Canberra.

GLEN, R. A. 2005. The Tasmanides of eastern Australia. *Terrane Processes at the Margins of Gondwana,* 246**,** 23-96.

GLEN, R. A. 2013. Refining accretionary orogen models for the Tasmanides of eastern Australia. *Australian Journal of Earth Sciences,* 60**,** 315-370.

GLEN, R. A., KORSCH, R. J., HEGARTY, R., SAEED, A., DJOMANI, Y. P., COSTELLOE, R. D. & BELOUSOVA, E. 2013. Geodynamic significance of the boundary between the Thomson Orogen and the Lachlan Orogen, northwestern New South Wales and implications for Tasmanide tectonics. *Australian Journal of Earth Sciences,* 60**,** 371-412.

GLEN, R. A., PERCIVAL, I. G. & QUINN, C. D. 2009. Ordovician continental margin terranes in the Lachlan Orogen, Australia: Implications for tectonics in an accretionary orogen along the east Gondwana margin. *Tectonics,* 28.

GRAY, D. R. & FOSTER, D. A. 2004. Tectonic evolution of the Lachlan Orogen, southeast Australia: historical review, data synthesis and modern perspectives. *Australian Journal of Earth Sciences,* 51**,** 773-817.

KENNETT, B. L. N., FISHWICK, S., READING, A. M. & RAWLINSON, N. 2004. Contrasts in mantle structure beneath Australia: relation to Tasman Lines? *Australian Journal of Earth Sciences,* 51**,** 563-569.

KENNETT, B. L. N., SALMON, M., SAYGIN, E. & GRP, A. W. 2011. AusMoho: the variation of Moho depth in Australia. *Geophysical Journal International,* 187**,** 946-958.

LASKE, G. 1997. A global digital map of sediment thickness. *Eos Trans. AGU,* 78**,** F483.

LEVSHIN, A. L. & RITZWOLLER, M. H. 2001. Automated detection, extraction, and measurement of regional surface waves. *Pure and Applied Geophysics,* 158**,** 1531-1545.

LI, G., CHEN, H., NIU, F., GUO, Z., YANG, Y. & XIE, J. 2016. Measurement of Rayleigh wave ellipticity and its application to the joint inversion of high-resolution S-wave velocity structure beneath northeast China. *Journal of Geophysical Research: Solid Earth,* 121**,** 864-880.

LIN, F. C., MOSCHETTI, M. P. & RITZWOLLER, M. H. 2008. Surface wave tomography of the western United States from ambient seismic noise: Rayleigh and Love wave phase velocity maps. *Geophysical Journal International,* 173**,** 281-298.

LIN, F. C., TSAI, V. C. & SCHMANDT, B. 2014. 3-D crustal structure of the western United States: application of Rayleigh-wave ellipticity extracted from noise cross-correlations. *Geophysical Journal International,* 198**,** 656-670.

MA, Y. R., CLAYTON, R. W. & LI, D. Z. 2016. Higher-mode ambient-noise Rayleigh waves in sedimentary basins. *Geophysical Journal International,* 206**,** 1634-1644.

MALISCHEWSKY, P. G. & SCHERBAUM, F. 2004. Love's formula and H/V-ratio (ellipticity) of Rayleigh waves. *Wave Motion,* 40**,** 57-67.

MORESI, L., BETTS, P. G., MILLER, M. S. & CAYLEY, R. A. 2014. Dynamics of continental accretion. *Nature,* 508**,** 245-+.

OLLIER, C. 1995. Tectonics and landscape evolution in southeast Australia. *Geomorphology,* 12**,** 37-44.

PAYNE, J. L., HAND, M., BAROVICH, K. M. & WADE, B. P. 2008. Temporal constraints on the timing of high-grade metamorphism in the northern Gawler Craton: implications for assembly of the Australian Proterozoic. *Australian Journal of Earth Sciences,* 55**,** 623-640.

PILIA, S., RAWLINSON, N., CAYLEY, R. A., BODIN, T., MUSGRAVE, R., READING, A. M., DIREEN, N. G. & YOUNG, M. K. 2015. Evidence of micro-continent entrainment during crustal accretion. *Scientific Reports,* 5.

PILIA, S., RAWLINSON, N., DIREEN, N. G., CUMMINS, P. R. & BALFOUR, N. 2013. Structural controls on localized intraplate deformation and seismicity in Southern Australia: Insights from local earthquake tomography of the Flinders Ranges. *Journal of Geophysical Research-Solid Earth,* 118**,** 2176-2190.

RAWLINSON, N. & FISHWICK, S. 2012. Seismic structure of the southeast Australian lithosphere from surface and body wave tomography. *Tectonophysics,* 572**,** 111-122.

RAWLINSON, N. & KENNETT, B. L. N. 2008. Teleseismic tomography of the upper mantle beneath the southern Lachlan Orogen, Australia. *Physics of the Earth and Planetary Interiors,* 167**,** 84-97.

RAWLINSON, N., KENNETT, B. L. N., VANACORE, E., GLEN, R. A. & FISHWICK, S. 2011. The structure of the upper mantle beneath the Delamerian and Lachlan orogens from simultaneous inversion of multiple teleseismic datasets. *Gondwana Research,* 19**,** 788-799.

RAWLINSON, N., PILIA, S., YOUNG, M., SALMON, M. & YANG, Y. 2016. Crust and upper mantle structure beneath southeast Australia from ambient noise and teleseismic tomography. *Tectonophysics,* 689**,** 143-156.

RAWLINSON, N., SALMON, M. & KENNETT, B. L. N. 2014. Transportable seismic array tomography in southeast Australia: Illuminating the transition from Proterozoic to Phanerozoic lithosphere. *Lithos,* 189**,** 65-76.

RITZWOLLER, M. H., LIN, F. C. & SHEN, W. S. 2011. Ambient noise tomography with a large seismic array. *Comptes Rendus Geoscience,* 343**,** 558-570.

SAYGIN, E. & KENNETT, B. L. N. 2010. Ambient seismic noise tomography of Australian continent. *Tectonophysics,* 481**,** 116-125.

SAYGIN, E. & KENNETT, B. L. N. 2012. Crustal structure of Australia from ambient seismic noise tomography. *Journal of Geophysical Research-Solid Earth,* 117.

SHAPIRO, N. M. & CAMPILLO, M. 2004. Emergence of broadband Rayleigh waves from correlations of the ambient seismic noise. *Geophysical Research Letters,* 31.

SHAPIRO, N. M., CAMPILLO, M., STEHLY, L. & RITZWOLLER, M. H. 2005. High-resolution surface-wave tomography from ambient seismic noise. *Science,* 307**,** 1615-1618.

SIMONS, F. J., ZIELHUIS, A. & VAN DER HILST, R. D. 1999. The deep structure of the Australian continent from surface wave tomography. *Lithos,* 48**,** 17-43.

TANIMOTO, T. & RIVERA, L. 2008. The ZH ratio method for long-period seismic data: sensitivity kernels and observational techniques. *Geophysical Journal International,* 172**,** 187-198.

TKALCIC, H., RAWLINSON, N., ARROUCAU, P., KUMAR, A. & KENNETT, B. L. N. 2012. Multistep modelling of receiver-based seismic and ambient noise data from WOMBAT array: crustal structure beneath southeast Australia. *Geophysical Journal International,* 189**,** 1681-1700.

WANG, L., HITCHMAN, A. P., OGAWA, Y., SIRIPUNVARAPORN, W., ICHIKI, M. & FUJI-TA, K. 2014. A 3-D conductivity model of the Australian continent using observatory and magnetometer array data. *Geophysical Journal International,* 198**,** 1143-1158.

WORKMAN, E., LIN, F. C. & KOPER, K. D. 2017. Determination of Rayleigh wave ellipticity across the Earthscope Transportable Array using single-station and array-based processing of ambient seismic noise. *Geophysical Journal International,* 208**,** 234-245.

YANG, Y. J., RITZWOLLER, M. H., LEVSHIN, A. L. & SHAPIRO, N. M. 2007. Ambient noise rayleigh wave tomography across Europe. *Geophysical Journal International,* 168**,** 259-274.

YOUNG, M. K., CAYLEY, R. A., MCLEAN, M. A., RAWLINSON, N., ARROUCAU, P. & SALMON, M. 2013. Crustal structure of the east Gondwana margin in southeast Australia revealed by transdimensional ambient seismic noise tomography. *Geophysical Research Letters,* 40**,** 4266-4271.

YOUNG, M. K., RAWLINSON, N., ARROUCAU, P., READING, A. M. & TKALCIC, H. 2011. High-frequency ambient noise tomography of southeast Australia: New constraints on Tasmania's tectonic past. *Geophysical Research Letters,* 38.